

## Response to the Reviews' Comments

We thank reviewers for providing insightful comments and helpful suggestions that have substantially improved the manuscript. Below we have included the reviewers' comments in italic followed by our responses in blue. In the revised manuscript, we have highlighted those changes accordingly with changes tracked.

### Reviewer #1:

*Comment 1:* The manuscript was improved through the revision. Most of my concerns have been addressed. However, there remains a major problem regarding the calculation of the volume fraction of black carbon (BC). This concern was initially raised in my major comment #1 on the original manuscript. In their responses, the authors argued that for a spherical particle, its mass-equivalent size equals its mobility size. I agree with this point. However, it has been well known that BC particles (i.e., BC cores) are non-spherical. Thus, for an internally mixed BC-containing particle, it is not proper to calculate the volume fraction of BC based on the mass-equivalent size of the BC core and the mobility size of the whole particle. Indeed, in Mie theory calculations, an internally mixed BC-containing particle is usually idealized as a two-component sphere with a concentric core-shell morphology. However, this does not necessarily mean that the mass-equivalent size equals the mobility size for the BC cores. I believe that the methodology used in this manuscript for the calculation of BC's volume fraction is not the common practice. Limitations and uncertainties associated with this methodology must be considered and explained clearly in the main manuscript. If this concern could be properly addressed, this manuscript should be able to be considered for publication in ACP as a special issue paper.

### Response:

Indeed, the BC particles are non-spherical in the atmosphere, especially in the case of freshly emitted BC particles. However, after atmospheric aging, BC particle can experience significant restructuring and become more compact (Pagels et al., 2009). This is also confirmed by direct observations using scanning transmission X-ray microscopy (Moffet et al., 2016). High-resolution transmission electron microscopy (TEM) measurements conducted at a nearby location (Hong Kong) also showed that soot core tend to be spherical (Zhou et al., 2014). In many global models, BC particles are considered as either completely externally- or internally-mixed. It is also strongly suggested that BC is more likely to assuming a core-shell configuration rather than being well-mixed with other components to more realistically represent BC in the atmosphere (Jacobson, 2000). BC particle measurement techniques are mainly based on BC's optical or thermo-optical properties, which are in principle independent from the BC morphology and mixing-state (see Table 1 in Bond et al. (2013)). Therefore, the BC mass concentration has to be derived under the assumption of concentric core-shell configuration. For example, the BC particle size and the corresponding coating thickness reported by SP2 (one of the most advanced BC instruments) is also BC volume equivalent diameter (90 - 250nm) assuming a spherical shape, and the quantitative uncertainty of this method is still not determined (Schwarz et al., 2008).

In this work, the BC-containing particle were found mostly aged biomass burning particles and thus it would be reasonable to assume they were in a compact core-shell configuration,

such that a Mie-calculation can be used. As suggested by the reviewer, the accuracy of the calculation results would be significantly affected by the non-sphericity of BC core, which was deduced from the particle mobility diameter and BC mass fraction as used by Cheng et al. (2006) and Ma et al. (2012) in their researches. Since the particle mobility diameter ( $D_p$ ) is also a function of the shape of the particle that would to some extent reflect the BC core shape, the error in  $D_p$  measurement will inherit the uncertainty induced by the BC core morphology. The BC mass was converted from BC optical absorption signals (Bond et al., 2013), the accuracy of which will be affected by the complex refractive index and BC material density used in the calculation. In order to evaluate the uncertainty associated with BC calculation using Mie code, Cheng et al. (2006) have conducted Mont Carlo simulation to systematically evaluate the uncertainties of BC absorption calculation in the cases of internal mixture and external mixture with results of  $\pm 10\%$  and  $\pm 8\%$ , respectively. To our best knowledge, this is the only systematic analysis of the uncertainty associated with Mie calculation that can be found in the literature. In the Mont Carlo simulation, a series of random numbers (or random error of each measurement) were applied to the input parameters of the Mie code and a sufficient number of repetition of the Mie calculation will be performed to guarantee the random errors are normally distributed. In this work, five hundred of runs were conducted. Table S1 listed one standard deviation ( $\sigma$ ) of each input parameter of the Mie calculation used in this work, i.e., the ranges of errors that were typically encountered in the field measurements using similar instrumentation as in our study. In order to exclude the possible effects of extreme values, we set the error range to be within  $\pm 3\sigma$ , which contained 99% possible values of the input parameters. Table S2 listed the Monte Carlo simulation results, i.e., the average relative standard deviations ( $\sigma_{\text{Mie}}$ ) of the calculated BC light absorption at 880 nm ( $\text{Abs}_{880}$ ),  $\text{AAE}_{\text{BC},370-520}$ , and  $\text{AAE}_{\text{BC},520-880}$ . The uncertainties of the calculated  $\text{Abs}_{880}$ ,  $\text{AAE}_{\text{BC},370-520}$ , and  $\text{AAE}_{\text{BC},520-880}$  at 2 times of  $\sigma_{\text{Mie}}$ , i.e., at a confidence coefficient of 95%, were approximately  $\pm 31\%$ ,  $\pm 16\%$ , and  $\pm 13\%$ , respectively. Figure S4 also showed the time series of the uncertainties of  $\text{Abs}_{880}$ ,  $\text{AAE}_{\text{BC},370-520}$  and  $\text{AAE}_{\text{BC},520-880}$  from Monte Carlo simulation for the campaign period.

**Table S1.** Uncertainties of each input parameter, which was given in terms of one relative standard deviation ( $\sigma$ ).

Parameters	$\pm\sigma$ (%)
$D_{p, \text{DMA}}$	1.2 <sup>a</sup>
$N_{\text{CPC}}$	3.3 <sup>a</sup>
$D_{p, \text{APS}}$	3.0 <sup>b</sup>
$N_{\text{APS}}$	3.3 <sup>b</sup>
$\tilde{m}_{\text{non}}=1.50$	0.3 <sup>c</sup>
$\tilde{m}_{r, \text{BC}}=1.80$	3.3 <sup>c</sup>
$\tilde{m}_{i, \text{BC}}=0.54$	13.3 <sup>c</sup>
$\rho_{\text{BC}}=1.5$	11 <sup>d</sup>

$$r_{\text{ext}}=0.58$$

$$45^{\circ}$$

$$\Phi_{N,CV}$$

$$20.7^f$$

<sup>a</sup> The measurement uncertainties of the DMA for  $D_{p,DMA}$  and the CPC for  $N_{CPC}$ , which were recommended by Wiedensohler et al. (2012).

<sup>b</sup> The measurement uncertainty of the APS and the uncertainty during the transformation from aerodynamic diameter to Stokes diameter recommended by Peters and Leith (2003).

<sup>c</sup> The uncertainties of the refractive indices of non-light absorbing materials and BC core recommended by Cheng et al. (2006).

<sup>d</sup> The uncertainty of  $\rho_{BC}$  at a 99% confidence level, ranging from  $1.00 \text{ g cm}^{-3}$  to  $2.00 \text{ g cm}^{-3}$  (Ma et al., 2012).

<sup>e</sup> The uncertainty of  $r_{\text{ext}}$  is taken from the optical closure study results of Tan et al. (2016).

<sup>f</sup> The uncertainty of  $\Phi_{N,CV}$  is evaluated from six diameters of the VTDMA measurement conducted in Guangzhou by Cheung et al. (2016).

**Table S2.** Averaged relative standard deviation ( $\sigma_{Mie}$ ) of the calculated  $Abs_{880}$ ,  $AAE_{BC,370-520}$ , and  $AAE_{BC,520-880}$  obtained from Monte Carlo simulations.

	$Abs_{880}$	$AAE_{BC,370-520}$	$AAE_{BC,520-880}$
$\sigma_{Mie}$ (%)	15.4	7.9	6.6

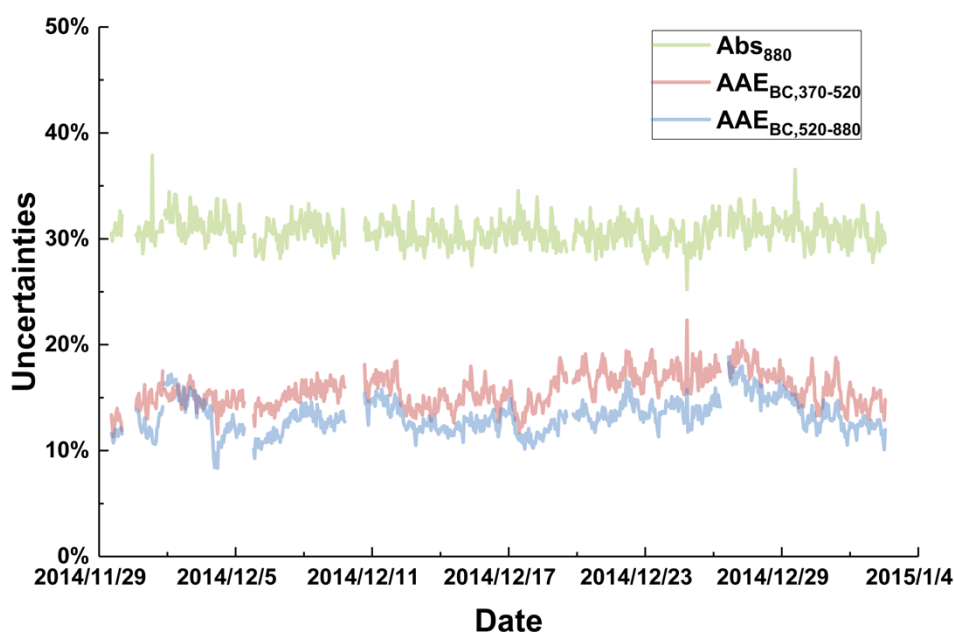


**Figure S5.** Time series of the uncertainties ( $2\sigma_{Mie}$ ) of  $Abs_{880}$ ,  $AAE_{BC,370-520}$ , and  $AAE_{BC,520-880}$  from Monte Carlo simulation.

In the manuscript, we have inserted the following discussion in Line 477:

“Furthermore, we have performed Monte Carlo simulations to evaluate the uncertainties of the Mie calculation performed during this work. In the simulation, a sequence of random numbers

or errors were applied to the input parameters, and then the corresponding uncertainties of particle light absorption and  $AAE_{BC}$  by were computed using the Mie model. Five hundred of reiteration were conducted during the simulation such that the random errors will be normally distributed. The standard deviations ( $\sigma$ ) of all input parameters are listed in Table S1. In order to cover the effect of extreme value, we used a range of  $\pm 3\sigma$ , or a confidence level of 99%, in the Monte Carlo simulation. Table S2 listed the Monte Carlo simulation results, i.e., the average relative standard deviations ( $\sigma_{Mie}$ ) of the calculated BC light absorption at 880 nm ( $Abs_{880}$ ),  $AAE_{BC,370-520}$ , and  $AAE_{BC,520-880}$ . The uncertainties of the calculated  $Abs_{880}$ ,  $AAE_{BC,370-520}$ , and  $AAE_{BC,520-880}$  at 2 times of  $\sigma_{Mie}$ , i.e., at a confidence coefficient of 95%, were approximately  $\pm 31\%$ ,  $\pm 16\%$ , and  $\pm 13\%$ , respectively. Figure S5 also showed the time series of the uncertainties of  $Abs_{880}$ ,  $AAE_{BC,370-520}$  and  $AAE_{BC,520-880}$  from Monte Carlo simulation for the campaign period.”

**Reviewer #2:**

**Comment 1:** “The authors have made a lot of efforts in addressing how the BC core has been calculated, however there is no plot to show this at all. It is mentioned that previous VTDMA measurements were conducted, would you like to show these results? would you like to show the BC core size distribution etc...”

Response:

As suggested by the reviewer, we have included the following information of VTDMA measurements in the manuscript. The VTDMA measurement refers to the study conducted at the same site of this study (Cheung et al., 2016; Tan et al., 2016). During the VTDMA measurements, particles with certain size selected by the first DMA were sent through a heater maintained at 300°C. The shrunk particles were then scanned by the second DMA. The particle volatility was defined as the shrinkage or the shrink factor measured by the TDMA system. It was defined as low volatility (LV), medium volatility (MV), and high volatility (HV) particles, respectively. In addition, some extreme volatile particles that were vaporized without any residuals at 300°C and thus were defined as the completely vaporized (CV) particles or  $\Phi_{N,CV}$  used in this work. The number fractions of these aforementioned four types of the particles were listed in following Table, which can be found in Cheung et al. (2016).

Diameter (nm)	40	80	110	150	200	300
Number fraction						
CV	0.380±0.153	0.174±0.097	0.188±0.081	0.167±0.074	0.153±0.070	0.141±0.065
HV	0.255±0.097	0.198±0.052	0.380±0.153	0.380±0.153	0.380±0.153	0.380±0.153
MV	0.314±0.097	0.513±0.089	0.515±0.098	0.530±0.105	0.523±0.116	0.497±0.125
LV	0.051±0.026	0.113±0.040	0.132±0.041	0.140±0.041	0.255±0.097	0.255±0.097

Accordingly, the  $\Phi_{N,CV}$  values taken for this work were 0.384, 0.181, 0.180, 0.158, 0.143 and 0.137, corresponding to 40, 80, 110, 150, 200 and 300 nm size bins, respectively, which can also be presented as a 6-bin distribution plot (Fig. S3):

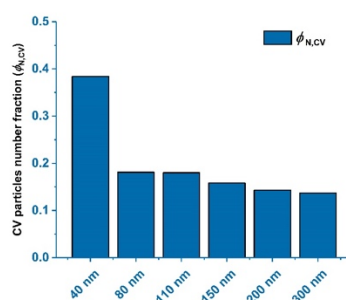


Figure S3. The size distribution of  $\Phi_{N,CV}$ .

In the manuscript, we have revised the statement as (Line 353):

“The average values were 0.384, 0.181, 0.180, 0.158, 0.143 and 0.137, corresponding to 40, 80, 110, 150, 200 and 300 nm, respectively, which were obtained from a previous study at the same site (Cheung et al., 2016; Tan et al., 2016). The size-independent  $\Phi_{N,CV}$  was interpolated linearly

with these six diameters. For particle size larger than 300 nm and less than 40 nm,  $\Phi_{N,CV}$  values were set to 0.137 and 0.384, respectively.”

**Comment 2:** “There are quite a few fundamental plots missing:

*Time series of AAE measured by AE33.*

*Time series of assumed/derived BC core size.*

*A total scattering, SSA.*

*An analysis of air mass origins to indicate the possible source influences on high loadings of OC.”*

Response:

As suggested by the reviewer, we have inserted the following figures into the SI as supporting information. Figure S1 shows the time series of aerosol extinction coefficients, scattering coefficients, and SSA at 532 nm. Figure S2 shows the time series of size distribution of the derived external BC and internal BC core. Figure S4 is the time series of particle AAE measured by the Aethalometer and  $AAE_{BC}$  derived by the Mie model calculation. To explore the origins of the air mass may be influenced by high loadings of OC, we have conducted 3-day backward trajectory analyses and the results are presented in Fig. S6.

In the manuscript, we added the statement as (Line 187):

“The corresponding time series of extinction coefficients, scattering coefficients, and SSA at 532 nm was displayed in Fig. S1.”

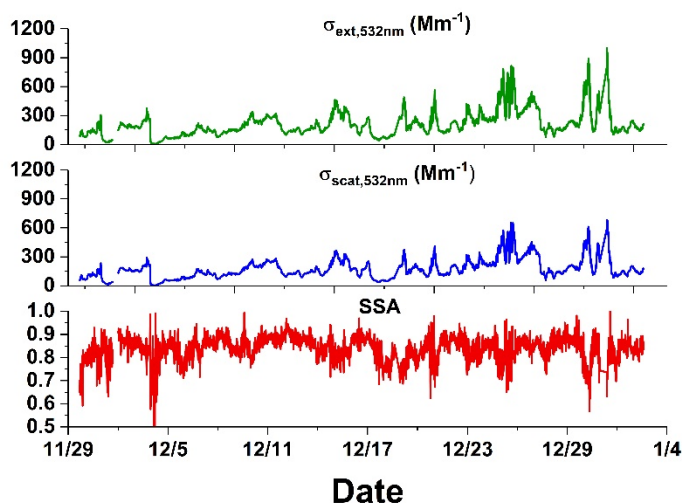


Figure S1. Time series of aerosol extinction coefficients, scattering coefficients and SSA at 532 nm.

In the manuscript, we added the statement as (Line 301):

“The corresponding time series of size distribution of the derived external BC and internal BC core were illustrated in Fig. S2.”

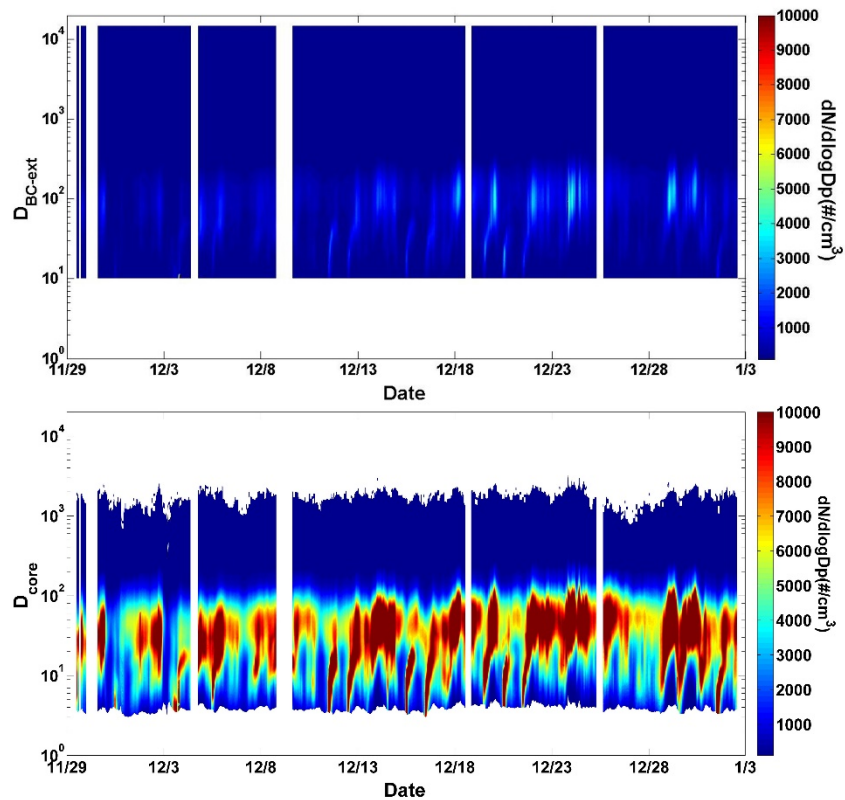


Figure S2. Time series of size distribution of the derived external BC and internal BC core.

In the manuscript, we revised the statement as (Line 394):

“Figure. S4 displayed the time series of particle AAE measured by the Aethalometer and  $AAE_{BC}$  was derived from Mie model calculation. The  $AAE_{BC}$  was almost always lower than AAE, indicating appreciable BrC light absorption at the Panyu site.”

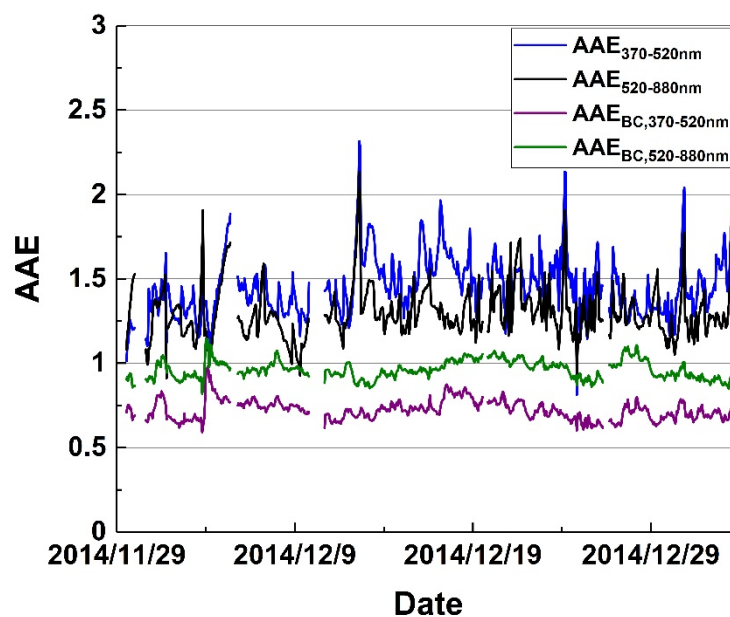


Figure S4. Time series of particle AAE measured by the Aethalometer and  $AAE_{BC}$  derived from

Mie model calculation.

In the manuscript, we added the statement as (Line 582):

“Figure S6 showed the 3-day backward trajectory and the fire counts for 5 to 7 (Fig. S6a), 12 to 14 (Fig. S6b) and 24 to 26 (Fig. S6c) in November 2014, representing low loading, moderate loading and high loading period. Clearly, the high loading period concurred with stagnant air movement and higher fire counts, indicating the contribution from open fire burning sources.”

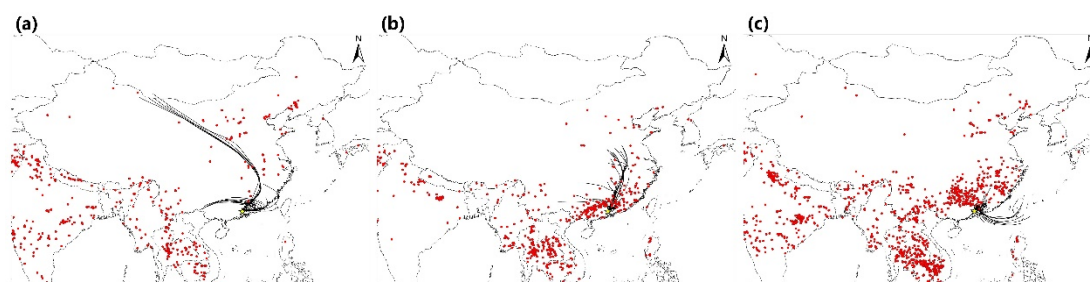


Figure S6. Map of 3-day backward trajectory and the fire counts for (a) 5 to 7 December 2014 (b) 12 to 14 December 2014 and (c) 24 to 26 December 2014. Fire count data were from the MODIS Collection 6 Active Fire Product in Fire Information for Resource Management System (FIRMS). Backward trajectories for the past 3-day were calculated using NOAA’s Hybrid Single Particle Lagrangian Integrated Trajectory (HYSPPLIT) model.

**Comment 3:** “A large section of texts and analysis to demonstrate that AAE could be subject to uncertainties resulting from core size, RI, Df etc. however there is no plot really showing that, not a model-only sensitivity plot, but some plots really showing your data. The model-only plot could be in supplement, but merge Fig. 3 and Fig. 4 by incorporating your data.”

*I don’t quite like Fig.3, would you like to show a time series of predicted AAE to indicate at which period the uncertainty could be large.*

Response:

Light absorption capacity of BC particles is one of the most important factors to predict BC radiative forcing effects during climate researches, which can be significantly affected by the presence of BrC. To separate the light absorption of BrC from that of BC, the exact values of  $AAE_{BC}$  are critically needed but, in theory, they cannot be measured directly.  $AAE_{BC}$  can be derived from BC light absorption measurements by an Aethalometer at different wavelengths under the assumption that light absorption of BrC has strong wavelength dependency. The derived values of  $AAE_{BC}$  ranged widely and their accuracy was rarely investigated in previous researches. A lot of factors, including the exact shape, size, refractive indices, and mixing state of BC particle can affect the true values of  $AAE_{BC}$  and these factors are usually taken from literature or adopted from the properties of pure BC material. Mie model with a core-shell configuration is by far the only practical way to realistically simulate and evaluate the potential errors induced by the uncertainties of the above factors. Therefore, we believe Fig. 3 and Fig. 4 are critically needed in the manuscript and they are based on different constraint conditions.

Merging them may lose some information. Nevertheless, as suggested by the reviewer we have included the measured  $AAE_{BC}$  time series (Fig. S4) in the SI section to show the actual data set. Furthermore, we have performed Monte Carlo simulations to evaluate the uncertainties of the Mie calculation performed during this work. In the simulation, a sequence of random numbers or errors were applied to the input parameters, and then the corresponding uncertainties of particle light absorption and  $AAE_{BC}$  by were computed using the Mie model. Five hundred of reiteration were conducted during the simulation such that the random errors will be normally distributed. The standard deviations ( $\sigma$ ) of all input parameters are listed in Table S1. In order to cover the effect of extreme value, we used a range of  $\pm 3\sigma$ , or a confidence level of 99%, in the Monte Carlo simulation. Table S2 listed the Monte Carlo simulation results, i.e., the average relative standard deviations ( $\sigma_{Mie}$ ) of the calculated BC light absorption at 880 nm ( $Abs_{880}$ ),  $AAE_{BC,370-520}$ , and  $AAE_{BC,520-880}$ . The uncertainties of the calculated  $Abs_{880}$ ,  $AAE_{BC,370-520}$ , and  $AAE_{BC,520-880}$  at 2 times of  $\sigma_{Mie}$ , i.e., at a confidence coefficient of 95%, were approximately  $\pm 31\%$ ,  $\pm 16\%$ , and  $\pm 13\%$ , respectively. Figure S5 also showed the time series of the uncertainties of  $Abs_{880}$ ,  $AAE_{BC,370-520}$  and  $AAE_{BC,520-880}$  from Monte Carlo simulation for the campaign period.

**Comment 4:** *In Fig. 8, there is no point to correlate BrC absorption with everything, again I would like to see a comprehensive time series to show the correlation at different periods.*

Response:

The similar trends among the time series of OC,  $K^+$ , and BrC absorption as shown in Fig. 5 strongly suggested that they may share similar origins. Therefore, we made Fig. 8 to further explore all possible BrC sources. As suggested by the reviewer, we have included more measurement data sets in the SI (e.g., Figs. S1-S3) to help readers to better understand the atmospheric conditions. To explore the correlations at different periods is a good suggestion. However, no clear correlation among BrC, Cl<sup>-</sup>, and other earth metals can be found at all, indicating that dusts and sea salts did not contribute to the light absorption. The back-trajectory analyses also pointed the origin of BrC to biomass burning events (see Fig. S6). Therefore, we consider Fig. 8 is very much necessary and sufficient to demonstrate the origin of BrC in this work.

**Comment 5:** “Have you got at least levoglucosan data, a  $K^+$ /levoglucosan may indicate possible different sources.”

Response:

We agree with the reviewer that levoglucosan can be a robust biomass burning tracer due to its unique formation mechanism. However, the measurement techniques for levoglucosan are very challenging and may be subject to many limitations (Bhattarai et al., 2019). Levoglucosan may also experience degradation after emission, which make it even more difficult to be accurately detected in the aged plumes. Potassium is also a well-established biomass burning tracer and has been extensively investigated by many field researches, including those to explore other possible  $K^+$  sources.  $K^+$  is relatively more abundant than levoglucosan and easier to be measured. It is also very stable during aging and transport of the plumes, which make it an ideal tracer for biomass burning event. Ideally, it would be better to have both tracers measured

during the field work such that they can be cross-checked. Unfortunately, we do not have levoglucosan measurement during this work. However, as recommended by previous reviewers, we have explored other possible  $K^+$  sources during this work (see Fig. S8 for details) and it was demonstrated to be very minor to the biomass burning emissions. Hence, we are confident that  $K^+$  was emitted from biomass burning events during the study period.

**Comment 6:** “There are many duplications between Fig. 7 and Fig. 9, would you merge some of the information and present only the important message neatly?”

Response:

We agree with the reviewer. Fig. 7b and Fig. 9a are basically the same. The purpose of Fig. 9 was to establish the possible source of BrC from biomass burning using  $K^+$  as a tracer. To avoid the duplication, we have removed Fig. 9 into the SI section (now Fig. S7) as a supporting information.

**Comment 7:** It is unnecessary to show all of the sensitivity analysis in Fig. 10.

Response:

In Fig.10 (now Fig. 9), we want to show the BrC radiative forcing efficiency ( $RFE_{BrC}$ ) under various SSA (ranging from 0.7 to 0.99) that can be encountered in the atmosphere in the study area. Especially, our study was done under dry conditions. The atmospheric RH may affect SSA significantly. Therefore, SSA under different ambient conditions should be considered during the calculation of  $RFE_{BrC}$  using the SBDART model. Thus, BrC light absorption contribution at all three wavelengths can be conveniently assessed through the three plots. Nevertheless, we appreciate the thoughtful suggestion from the reviewer.

**Comment 8:** Regarding how far this paper could go, I think at least one useful key message should be delivered, not just simply report how much BrC could occupy in shorter wavelength. I would think you could point out at this southern coastal site during this season, how much AAE could reach, what the general background look like, how important could the BrC there compared to other places over China. Are those BrC from fire or just anthropogenic?

Response:

That is a very insightful comment. As suggested by the reviewer, we have included other important observation datasets into the SI for references. The AAE and  $AAE_{BC}$  are shown in Fig. S4. For ambient particles,  $AAE_{370-520nm}$  and  $AAE_{520-880nm}$  ranged from 0.81 to 2.31 and 0.91 to 2.13, respectively. In the case of BC,  $AAE_{BC,370-520nm}$  and  $AAE_{BC,520-880nm}$  ranged from 0.59 to 0.98 and 0.82 to 1.15, respectively. The research period (Nov 2014) was a low PM loading period, which can be considered as the background level in the studied area. During this period, the averaged  $AAE_{370-520nm}$  and  $AAE_{520-880nm}$  was 1.47 and 1.34, respectively, which was also relatively lower than other similar studies (Wang et al., 2018).

In Table 2, we have listed field studies of the BrC light absorption coefficient and BrC light absorption contribution in the near-ultraviolet wavelength range in East Asia region, including China. The reported values vary substantially, and our result is toward the lower end in BrC

light absorption coefficient but the high end of contribution to light absorption.

In this work, BrC was mainly originated from biofuel burning process, including the open fire burning and domestic activities, indicated by the high  $K^+$  level in the samples. Further research including more chemical analysis techniques may help us to pin down the exact type of biomass burning.

We have inserted the following statement into the conclusion section:

Line 702: “The AAE of ambient particles and BC core were derived from the measurements. For ambient particles,  $AAE_{370-520nm}$  and  $AAE_{520-880nm}$  ranged from 0.81 to 2.31 and 0.91 to 2.13, respectively. In the case of BC,  $AAE_{BC,370-520nm}$  and  $AAE_{BC,520-880nm}$  ranged from 0.59 to 0.98 and 0.82 to 1.15, respectively.”

Line 726: “Compared to the values of BrC light absorption coefficient and BrC light absorption contribution from other similar studies conducted in the East Asia region, the BrC measured in this work showed relatively lower values of light absorption coefficient but was found responsible for relatively higher portion of light absorption.”

#### References:

Pagels, J., Khalizov, A. F., McMurry, P. H., and Zhang, R. Y.: Processing of Soot by Controlled Sulphuric Acid and Water Condensation Mass and Mobility Relationship, *Aerosol Sci. Technol.*, 43, 629-640, 10.1080/02786820902810685, 2009.

Moffet, R. C., and Brien, R. E., Alpert, P. A., Kelly, S. T., Pham, D. Q., Gilles, M. K., Knopf, D. A., and Laskin, A.: Morphology and mixing of black carbon particles collected in central California during the CARES field study, *Atmospheric Chemistry and Physics*, 16, 14515-14525, 10.5194/acp-16-14515-2016, 2016.

Zhou, S., Wang, T., Wang, Z., Li, W., Xu, Z., Wang, X., Yuan, C., Poon, C. N., Louie, P. K. K., Luk, C. W. Y., and Wang, W.: Photochemical evolution of organic aerosols observed in urban plumes from Hong Kong and the Pearl River Delta of China, *Atmospheric Environment*, 88, 219-229, 10.1016/j.atmosenv.2014.01.032, 2014.

Jacobson, M. Z.: A physically-based treatment of elemental carbon optics: Implications for global direct forcing of aerosols, *Geophys. Res. Letts.*, 27, 217-220, doi:10.1029/1999GL010968, 2000.

Bond, T. C., Doherty, S. J., Fahey, D. W., Forster, P. M., Berntsen, T., DeAngelo, B. J., Flanner, M. G., Ghan, S., Karcher, B., Koch, D., Kinne, S., Kondo, Y., Quinn, P. K., Sarofim, M. C., Schultz, M. G., Schulz, M., Venkataraman, C., Zhang, H., Zhang, S., Bellouin, N., Guttikunda, S. K., Hopke, P. K., Jacobson, M. Z., Kaiser, J. W., Klimont, Z., Lohmann, U., Schwarz, J. P., Shindell, D., Storelvmo, T., Warren, S. G., and Zender, C. S.: Bounding the role of black carbon in the climate system: A scientific assessment, *J. Geophys. Res. Atmos.*, 118, 5380-5552, 10.1002/jgrd.50171, 2013.

Schwarz, J. P., Gao, R. S., Spackman, J. R., Watts, L. A., Thomson, D. S., Fahey, D. W., Ryerson,

T. B., Peischl, J., Holloway, J. S., Trainer, M., Frost, G. J., Baynard, T., Lack, D. A., de Gouw, J. A., Warneke, C., and Del Negro, L. A.: Measurement of the mixing state, mass, and optical size of individual black carbon particles in urban and biomass burning emissions, *Geophys. Res. Letts.*, 35, 10.1029/2008gl033968, 2008.

Cheng, Y. F., Eichler, H., Wiedensohler, A., Heintzenberg, J., Zhang, Y. H., Hu, M., Herrmann, H., Zeng, L. M., Liu, S., Gnauk, T., Brüggemann, E., and He, L. Y.: Mixing state of elemental carbon and non-light-absorbing aerosol components derived from in situ particle optical properties at Xinken in Pearl River Delta of China, *Journal of Geophysical Research: Atmospheres*, 111, doi:10.1029/2005JD006929, 2006.

Ma, N., Zhao, C. S., Müller, T., Cheng, Y. F., Liu, P. F., Deng, Z. Z., Xu, W. Y., Ran, L., Nekat, B., van Pinxteren, D., Gnauk, T., Müller, K., Herrmann, H., Yan, P., Zhou, X. J., and Wiedensohler, A.: A new method to determine the mixing state of light absorbing carbonaceous using the measured aerosol optical properties and number size distributions, *Atmos. Chem. Phys.*, 12, 2381-2397, 10.5194/acp-12-2381-2012, 2012.

Wiedensohler, A., Birmili, W., Nowak, A., Sonntag, A., Weinhold, K., Merkel, M., Wehner, B., Tuch, T., Pfeifer, S., Fiebig, M., Fjaraa, A. M., Asmi, E., Sellegri, K., Depuy, R., Venzac, H., Villani, P., Laj, P., Aalto, P., Ogren, J. A., Swietlicki, E., Williams, P., Roldin, P., Quincey, P., Hüglin, C., Fierz-Schmidhauser, R., Gysel, M., Weingartner, E., Riccobono, F., Santos, S., Gruning, C., Faloon, K., Beddows, D., Harrison, R. M., Monahan, C., Jennings, S. G., O'Dowd, C. D., Marinoni, A., Horn, H. G., Keck, L., Jiang, J., Scheckman, J., McMurry, P. H., Deng, Z., Zhao, C. S., Moerman, M., Henzing, B., de Leeuw, G., Loschau, G., and Bastian, S.: Mobility particle size spectrometers: harmonization of technical standards and data structure to facilitate high quality long-term observations of atmospheric particle number size distributions, *Atmos. Meas. Tech.*, 5, 657-685, 10.5194/amt-5-657-2012, 2012.

Peters, T. M., and Leith, D.: Concentration measurement and counting efficiency of the aerodynamic particle sizer 3321, *J. Aerosol Sci.*, 34, 627-634, [https://doi.org/10.1016/S0021-8502\(03\)00030-2](https://doi.org/10.1016/S0021-8502(03)00030-2), 2003.

Tan, H., Liu, L., Fan, S., Li, F., Yin, Y., Cai, M., and Chan, P. W.: Aerosol optical properties and mixing state of black carbon in the Pearl River Delta, China, *Atmos. Environ.*, 131, 196-208, <https://doi.org/10.1016/j.atmosenv.2016.02.003>, 2016.

Cheung, H. H. Y., Tan, H., Xu, H., Li, F., Wu, C., Yu, J. Z., and Chan, C. K.: Measurements of non-volatile aerosols with a VTDMA and their correlations with carbonaceous aerosols in Guangzhou, China, *Atmospheric Chemistry and Physics*, 16, 8431-8446, 10.5194/acp-16-8431-2016, 2016.

Bhattacharai, H., Saikawa, E., Wan, X., Zhu, H., Ram, K., Gao, S., Kang, S., Zhang, Q., Zhang, Y., Wu, G., Wang, X., Kawamura, K., Fu, P., and Cong, Z.: Levoglucosan as a tracer of biomass burning: Recent progress and perspectives, *Atmos. Res.*, 220, 20-33, <https://doi.org/10.1016/j.atmosres.2019.01.004>, 2019.

Wang, J., Nie, W., Cheng, Y., Shen, Y., Chi, X., Wang, J., Huang, X., Xie, Y., Sun, P., Xu, Z., Qi, X., Su, H., and Ding, A.: Light absorption of brown carbon in eastern China based on 3-year multi-wavelength aerosol optical property observations and an improved absorption Ångström exponent segregation method, *Atmospheric Chemistry and Physics*, 18, 9061-9074, 10.5194/acp-18-9061-2018, 2018.

1 **Light absorption properties and potential sources of particulate brown carbon in**  
2 **the Pearl River Delta region of China**

3  
4 Zhujie Li<sup>1,2</sup>, Haobo Tan<sup>2\*</sup>, Jun Zheng<sup>1\*</sup>, Li Liu<sup>2,3</sup>, Yiming Qin<sup>4</sup>, Nan Wang<sup>2</sup>, Fei Li<sup>2</sup>, Yongjie  
5 Li<sup>5</sup>, Mingfu Cai<sup>3</sup>, Yan Ma<sup>1</sup>, and Chak K. Chan<sup>4</sup>

6  
7 <sup>1</sup>Collaborative Innovation Center of Atmospheric Environment and Equipment Technology,  
8 Nanjing University of Information Science and Technology, Nanjing, China

9 <sup>2</sup>Key Laboratory of Regional Numerical Weather Prediction, Institute of Tropical and Marine  
10 Meteorology, China Meteorological Administration, Guangzhou, China

11 <sup>3</sup>Department of Atmospheric Science, Sun yat-sen University, Guangzhou, China

12 <sup>4</sup>School of Energy and Environment, City University of Hong Kong, Hong Kong, China

13 <sup>5</sup>Department of Civil and Environmental Engineering, Faculty of Science and Technology,  
14 University of Macau, Macau, China

15  
16 *Correspondence to: Haobo Tan (hbtan@grmc.gov.cn) and Jun Zheng (zheng.jun@nuist.edu.cn)*  
17  
18

19 **Abstract:**

20 Brown carbon (BrC) is a special type of organic aerosols (OA), capable of absorbing solar  
21 radiation from near-ultraviolet (UV) to visible wavelengths, which may lead to an increased  
22 aerosol radiative effect in the atmosphere. While high concentrations of OAs have been  
23 observed in the Pearl River Delta (PRD) region of China, the optical properties and  
24 corresponding radiative forcing of BrC in the PRD are still not well understood. In this work,  
25 we conducted a set of comprehensive measurements of atmospheric particulate matter from 29  
26 November 2014 to 2 January 2015 to investigate aerosol compositions, optical properties,  
27 source origins and radiative forcing effects at a suburban station in Guangzhou. The particle  
28 absorption Ångström exponent (AAE) was deduced and utilized to differentiate light absorption  
29 by BrC from that by black carbon (BC). The results showed that the average absorption  
30 contributions of BrC were  $34.1 \pm 8.0\%$  at 370 nm,  $23.7 \pm 7.3\%$  at 470 nm,  $16.0 \pm 6.7\%$  at 520 nm,  
31  $13.0 \pm 5.4\%$  at 590 nm and  $8.7 \pm 4.3\%$  at 660 nm. A sensitivity analysis of the evaluation of the  
32 absorption Ångström exponent of BC ( $AAE_{BC}$ ) was conducted based on the Mie theory  
33 calculation assuming that the BC-containing aerosol was mixed with the core-shell and external  
34 configurations. The corresponding uncertainty in  $AAE_{BC}$  was acquired. We found that  
35 variations in the imaginary refractive index (RI) of the BC core can significantly affect the  
36 estimation of  $AAE_{BC}$ . However,  $AAE_{BC}$  was relatively less sensitive to the real part of the RI  
37 of the BC core and was least sensitive to the real part of the RI of the nonlight absorbing shell.  
38 BrC absorption was closely related to aerosol potassium cation content ( $K^+$ ), a common tracer  
39 of biomass burning emissions, which was most likely associated with straw burning in the rural  
40 area of the western PRD. Diurnal variation in BrC absorption revealed that primary organic  
41 aerosols had a larger BrC absorption capacity than secondary organic aerosols (SOAs).  
42 Radiative transfer simulations showed that BrC absorption may cause  $2.3 \pm 1.8 \text{ W m}^{-2}$  radiative  
43 forcing at the top of the atmosphere (TOA) and contribute to  $15.8 \pm 4.4\%$  of the aerosol warming  
44 effect. A chart was constructed to conveniently assess the BrC radiative forcing efficiency in  
45 the studied area with reference to certain aerosol single-scattering albedo ( $SSA$ ) and BrC  
46 absorption contributions at various wavelengths. Evidently, the BrC radiative forcing efficiency  
47 was higher at shorter wavelengths.

**Keywords:** Brown carbon, Black carbon, Absorption Ångström exponent, Radiative forcing, Pearl River Delta.

## 48 **1 Introduction**

49 Black carbon (BC) and organic carbon (OC) are dominant carbonaceous aerosol components  
50 that mainly originate from biomass burning in a global scale (Bond et al., 2004) and have  
51 attracted great environmental concerns in rapidly developing regions. Carbonaceous aerosols  
52 can not only exert adverse impacts on public health, similar to other particulate matters, but  
53 also significantly affect the terrestrial radiation balance with enormous uncertainties. In  
54 previous studies, BC was often considered to be the only light-absorbing species (Andreae and  
55 Gelencser, 2006), and OC was believed to only be able to scatter light, i.e., causing a cooling  
56 effect (Bond et al., 2011). Nevertheless, it has been reported that some fraction of organic  
57 aerosols (OAs) may also specifically contribute to light absorption from the near-ultraviolet  
58 (UV) to visible wavelength range, which is referred to as brown carbon (BrC) (Kirchstetter et  
59 al., 2004). BrC optical properties are strongly affected by its chemical composition and physical  
60 structure, which are related to different BrC sources. BrC can originate not only from direct  
61 emissions, including smoldering, biomass burning or any type of incomplete fuel combustion  
62 process (T. C. Bond et al., 1999; Cheng et al., 2011), but also from secondary organic aerosol  
63 formation processes, such as aqueous phase reactions in acidic solutions (Desyaterik et al., 2013)  
64 or volatile organic compound (VOC) oxidation (Laskin et al., 2015; Sareen et al., 2010). In  
65 addition, BrC could have a complicated molecular composition and intermix with other  
66 substances, such as BC, non-absorbing OAs and other inorganic materials, making it  
67 complicated to investigate BrC optical properties.

68 BC absorption is commonly assumed to be covering the full wavelength-range. However, the  
69 light absorption property of BrC is believed to be more wavelength-dependent, which can be  
70 represented by distinct absorption Ångström exponent (AAE) values, i.e., the power exponent  
71 of the light absorption coefficient. A typical threshold for the AAE of BC (AAE<sub>BC</sub>) of 1.6 has  
72 been recommended to distinguish BrC from BC (Lack and Cappa, 2010), and the AAE of BrC  
73 has been reported as having a wider range (2 to 7) (Hoffer et al., 2005). Based on the difference  
74 in the wavelength dependence of light absorption between BC and BrC, previous studies have

75 applied the AAE method to differentiate light absorption by BrC through multiwavelength  
76 optical measuring apparatus, such as 3-wavelength Photoacoustic Soot Spectrometer (PASS-3)  
77 (Lack and Langridge, 2013), multiwavelength Aethalometer (Olson et al., 2015), etc. Based on  
78 the AAE method, the BrC absorption contribution has been estimated to be approximately 6 to  
79 41% of total aerosol light absorption at short wavelengths, e.g., at 370 nm and 405 nm  
80 (Washenfelder et al., 2015). A uniform  $AAE_{BC}$  from ~300 nm up to ~700 nm (Moosmüller et  
81 al., 2011) is commonly used when evaluating the BrC absorption contribution using the AAE  
82 method. However, it has been reported that the  $AAE_{BC}$  can be influenced by the mixing state,  
83 BC core size and morphology (Lack and Cappa, 2010). The lensing effect of the coating shell  
84 may enhance BC light absorption, the magnitude of which may also depend on wavelength and  
85 can alter the value of  $AAE_{BC}$  (Liu et al., 2018). Moreover, different values of  $AAE_{BC}$  have been  
86 found in the near-infrared and UV ranges (Wang et al., 2018). Therefore, using the default value  
87 of  $AAE_{BC} = 1$  may lead to uncertainty in BrC absorption coefficient estimation.

88 Quantifying BrC optical absorption accurately is essential to interpret aerosol optical depth  
89 (AOD), and the corresponding aerosol direct radiative forcing (DRF) on the atmosphere can  
90 also be evaluated if the single-scattering albedo (*SSA*) and extinction coefficient of aerosols are  
91 known. The estimation of the DRF of BrC has shown a distinct seasonal variation, indicating  
92 the influence of different absorption properties of BrC (Arola et al., 2015). A global simulation  
93 study indicated that the average warming effect at the TOA caused by BrC absorption can be  
94 up to  $0.11 \text{ W m}^{-2}$ , corresponding to ~25% of that predicted from BC absorption only (Feng et  
95 al., 2013).

96 During the last three decades, rapid economic development has led to severe air pollution  
97 problems in the PRD region (Chan and Yao, 2008). With rapid increases in the automobile  
98 population and factories, high loadings of SOAs have often been observed (Tan et al., 2016b).  
99 Biofuel usage may also play a significant role during wintertime air pollution events in the PRD,  
100 indicating that the contribution from BrC light absorption cannot be ignored (Wu et al., 2018).  
101 Recently, BrC light absorption has been quantified by Qin et al. (2018) using the AAE method  
102 in the PRD region. OA chemical composition was simultaneously measured by a high-  
103 resolution time-of-flight aerosol mass spectrometer, and it was found that organic aerosols  
104 originating from biomass burning possessed the most intense absorption capability and were

105 largely responsible for BrC absorption. Qin et al. (2018) also suggested that correlations  
106 between OA chemical compositions and BrC absorption were wavelength-dependent.

107 In this paper, we applied the homologous AAE differentiation method to quantify the fraction  
108 of aerosol light absorption by BrC using the measurements from a seven-wavelength  
109 Aethalometer. The potential error incurred with this methodology was determined using Mie  
110 theory simulations, especially for various complex refractive indexes of the BC core and the  
111 coating material. The correlation between BrC light absorption and water-soluble ions, which  
112 is used as the source tracer, was employed to identify potential BrC sources. An atmospheric  
113 radiative transfer model has also been applied to evaluate the impact of BrC on direct radiative  
114 forcing using surface-based aerosol optical properties and satellite-based surface-albedo data.  
115 The magnitudes of aerosol radiative forcing at the top of the atmosphere due to BC and BrC  
116 were also individually quantified.

## 117 **2 Methodology**

### 118 **2.1 Sampling site**

119 Field observations were conducted at the Panyu station (113°21'E, 23°00'N), which is a  
120 monitoring site of the Chinese Meteorological Administration (CMA) Atmospheric Watch  
121 Network (CAWNET) that is located on the summit of Dazhengang Mountain (approximately  
122 150 m above sea level) in Guangzhou, China. Figure 1 shows the location of the Panyu site,  
123 which is situated at the center of the PRD and is separated from residential areas by at least 500  
124 m. Some agricultural fields can be found to the west of the site. Although there were no  
125 significant pollution sources nearby, this suburban site was strongly affected by pollutants  
126 transported from the urban area of Guangzhou and crop residual fires transported from the rural  
127 area of the PRD. The field campaign was conducted from 29 November 2014 to 2 January 2015.  
128 During the measurement period, aerosol light scattering and extinction, BC concentration,  
129 particle number size distribution (PNSD), OC concentration, and the water-soluble ion  
130 concentrations of PM<sub>2.5</sub> were continuously monitored.

### 131 **2.2 Measurements and data analysis**

132 All instruments were housed inside the 2<sup>nd</sup> floor measurement room of a ~5-m tall, 2-story  
133 building. The ambient sample was taken on the roof by a 2-m long, 12.7-mm OD stainless steel  
134 inlet, and a PM<sub>2.5</sub> cyclone sampler was also used. The metal tubing was thermally insulated and

135 maintained at a constant temperature of  $\sim 25^{\circ}\text{C}$ . A diffusion drier was also used in-line to dry  
136 the relative humidity (RH) of the air sample below 30% before further analysis.

### 137 **2.2.1 Measurements of relevant species**

138 A TSI-3936 scanning mobility particle sizer (SMPS) and a TSI-3321 aerodynamic particle sizer  
139 (APS) were utilized to measure the 10 to 500 nm mobility diameter and 0.5 to 2.5  $\mu\text{m}$   
140 aerodynamic diameter of the PNSD, respectively. The aerodynamic diameters of the APS data  
141 were converted into mobility diameters using a material density of  $1.7\text{ g cm}^{-3}$ . A detailed data  
142 merging method has been described by Cheng et al. (2006). Furthermore, the pipe diffusion  
143 loss of SMPS has been corrected using the empirical formula proposed by Kulkarni et al. (1996).  
144 An AE-33 Aethalometer (Magee Scientific Inc.) was utilized for BC mass concentration  
145 measurement, which was derived from optical attenuation using a mass absorption cross section  
146 (MAC) of  $7.77\text{ m}^2\text{ g}^{-1}$  at 880 nm. The sensitivity of AE-33 was approximately  $0.03\text{ }\mu\text{g m}^{-3}$  for  
147 a 1-min time resolution and a 5.0 liter per minute (LPM) sample flow rate.

148 The  $\text{PM}_{2.5}$  mass concentration was measured by an Environment Dust Monitor (Model  
149 EDM180, GRIMM Inc.), which monitored the mass concentration of  $\text{PM}_{2.5}$  and  $\text{PM}_{10}$   
150 simultaneously.

151 Water-soluble ions (potassium ( $\text{K}^+$ ), calcium ( $\text{Ca}^{2+}$ ), magnesium ( $\text{Mg}^{2+}$ ), chloride ( $\text{Cl}^-$ ), sulfate  
152 ( $\text{SO}_4^{2-}$ ), nitrate ( $\text{NO}_3^-$ ), and ammonium ( $\text{NH}_4^+$ ) were measured with the Monitor for AeRosols  
153 and Gases in Air (MARGA) (Model ADI2080, Metrohm Inc.), which is an online analyzer for  
154 semi-continuous measurements of gases and water-soluble ions in aerosols (Li et al., 2010).

155 The MARGA was automatically calibrated with standard internal solutions during field  
156 measurement. The MARGA utilized its own  $\text{PM}_{2.5}$  sampling system provided by the  
157 manufacturer.

158 The OC mass concentration was measured by a Sunset online OC/EC analyzer (Model RT-4)  
159 with a laser transmittance-based charring correction (Wu et al., 2018). The sample flow rate of  
160 the OC/EC analyzer was maintained at 8 LPM. For each measurement cycle (one hour),  
161 samples were collected onto a quartz filter within the first 45 min and then thermal-optically  
162 analyzed during the remaining 15 min. First, OC was completely volatilized in oxygen-free  
163 helium with a stepwise ramped temperature (600  $^{\circ}\text{C}$  and 840  $^{\circ}\text{C}$ ). In the second stage, the  
164 temperature was reduced to 550  $^{\circ}\text{C}$ , and then EC and pyrolyzed carbon (PC) were combusted

165 in an oxidizing atmosphere (10% oxygen in helium), while the temperature was increased up  
 166 to 870 °C step by step. The CO<sub>2</sub> converted from all of the carbon components was then  
 167 quantified by a nondispersive infrared absorption CO<sub>2</sub> sensor (Lin et al., 2009). An internal  
 168 calibration peak made by 5% methane in helium was applied to quantify OC and EC. To correct  
 169 the PC converted from OC to EC, a tunable pulsed diode laser beam was used to monitor the  
 170 laser transmittance through the quartz filter throughout the thermal-optical analysis (Bauer et  
 171 al., 2012).

## 172 2.2.2 Measurements of optical properties

173 Light extinction by aerosols at 532 nm was detected using a cavity ring-down aerosol extinction  
 174 spectrometer (CRDS) (Model XG-1000, Hexin Inc.) by measuring the decay times of laser  
 175 intensity through the aerosol-containing sample and the filtered background air sample under  
 176 the same conditions. The extinction coefficient ( $\sigma_{ext}$ ) was calculated using the procedure  
 177 described by Khalizov et al. (2009).

178 Aerosol total scattering ( $\sigma_{sp}$ ) was measured by a TSI-3563 integrated nephelometer at three  
 179 wavelengths (i.e., 450 nm, 550 nm, and 700 nm) and was calibrated with CO<sub>2</sub> following the  
 180 manual instructions. Particle free air was used to check the nephelometer background signal  
 181 once every two hours. The scattering coefficients at other wavelengths were extrapolated using  
 182 the following equations:

$$183 \quad SAE = -\frac{\ln(\sigma_{scat,\lambda_0}) - \ln(\sigma_{scat,550nm})}{\ln(\lambda_0) - \ln(550)} \quad (1)$$

$$184 \quad \sigma_{scat}(\lambda) = \sigma_{scat}(550) \cdot \left(\frac{\lambda}{550}\right)^{-SAE} \quad (2)$$

185 where  $\lambda_0=450$  nm is for wavelengths less than 550 nm and  $\lambda_0=700$  nm is for wavelengths greater  
 186 than 550 nm. [The corresponding time series of extinction coefficients, scattering coefficients,  
 187 and SSA at 532 nm was displayed in Fig. S1.](#)

188 The Aethalometer is also used for multi-wavelength light absorption measurements in this study.  
 189 The seven-wavelength aerosol light attenuation coefficients ( $\sigma_{ATN}$ ) were converted into aerosol  
 190 light absorption coefficients ( $\sigma_{abs}$ ) using Eq. (3) (Coen et al., 2010), where  $k$  is the parameter  
 191 that accounts for the loading effect, ATN is the light attenuation through the filter with sample  
 192 loading and  $C_{ref}$  is a fixed multiple scattering parameter.

$$193 \quad \sigma_{abs} = \frac{\sigma_{ATN}}{(1-k \cdot ATN) \cdot C_{ref}} \quad (3)$$

194 The real-time  $k$  value was retrieved using the dual-spot loading correction algorithm developed  
 195 by Drinovec et al. (2015). The detailed formula of ATN can also be found in Drinovec et al.  
 196 (2015).  $C_{ref}$  is considered a constant that strongly depends on the filter matrix effect. However,  
 197 some studies have suggested that  $C_{ref}$  may vary with wavelength (Arnott et al., 2005; Segura et al.,  
 198 2014). For internal combustion engines and biomass burning,  $C_{ref}$  at 370 nm was expected to be  
 199 approximately 12% and 18% less than  $C_{ref}$  at 532 nm for the aerosol component, respectively  
 200 (Schmid et al., 2006). Different ambient observations also showed that  $C_{ref}$  may have regional  
 201 specificity, even though it was retrieved by the same methodology (Coen et al., 2010). In this  
 202 study,  $C_{ref}=3.29$  was used in Eq. (3) at each wavelength, and this value was derived from the  
 203 slope of  $\sigma_{ATN}$  measured by the Aethalometer vs.  $\sigma_{abs}$ , which was deduced from the CRDS and  
 204 nephelometer measurements. This  $C_{ref}$  was also very similar to the  $C_{ref}$  of 3.48 determined from  
 205 an inter-comparison study between an Aethalometer and a photoacoustic soot spectrometer  
 206 during a field campaign conducted in the PRD region in 2004 (Wu et al., 2009).

207 The BC light absorption at certain wavelengths was derived from the absorption coefficient  $\sigma_{abs}$   
 208 according to Beer-Lambert's law, and its variation between different pairs of wavelengths (i.e.,  
 209  $\sigma_{abs,BC,\lambda}$ ) is denoted by the absorption Ångström exponent (AAE) equation developed by  
 210 Ångström (1929):

$$211 \quad \sigma_{abs,BC,\lambda} = \sigma_{abs,BC,\lambda_0} \times (\lambda_0 / \lambda)^{-AAE_{BC}} \quad (4)$$

212 It has been suggested that the AAE of BC may vary between short and long wavelength ranges  
 213 (Lack and Cappa, 2010); hence, applying a wavelength-independent  $AAE_{BC}$  may lead to  
 214 uncertainties in the BC absorption calculation from one wavelength to another. In this work,  
 215 the light absorptions of BC at various wavelengths were retrieved by a modified wavelength-  
 216 dependent AAE differentiation method conducted by Wang et al. (2018):

$$217 \quad \sigma_{abs,BC,\lambda_1} = \sigma_{abs,BC,880nm} \times \left(\frac{880}{\lambda_1}\right)^{AAE_{BC,520-880nm}} \quad (5.1)$$

$$218 \quad \sigma_{abs,BC,\lambda_2} = \sigma_{abs,BC,880nm} \times \left(\frac{880}{520}\right)^{AAE_{BC,520-880nm}} \times \left(\frac{520}{\lambda_2}\right)^{AAE_{BC,370-520nm}} \quad (5.2)$$

219 Here,  $\sigma_{abs,BC,\lambda_1}$  represents the absorption coefficient due to only BC greater than 520 nm, and  
 220  $\sigma_{abs,BC,\lambda_2}$  represents the absorption coefficient of BC less than 520 nm.  $AAE_{BC,\lambda_i-\lambda_{i+1}}$  ( $i=1, 2$   
 221 and 3) represents the AAE of BC between a longer and shorter wavelength at  $\lambda_i=880, 520$  and  
 222 370 nm and was calculated as:

$$AAE_{BC,\lambda-\lambda_{i+1}} = -\frac{\ln(\sigma_{abs,BC,\lambda}) - \ln(\sigma_{abs,BC,\lambda_{i+1}})}{\ln(\lambda_i) - \ln(\lambda_{i+1})} \quad (6)$$

224 Accordingly, BrC absorption at a certain wavelength  $\lambda$  ( $\sigma_{abs,BrC,\lambda}$ ) was equal to the value of total  
225 aerosol absorption ( $\sigma_{abs,\lambda}$ ) minus BC absorption ( $\sigma_{abs,BC,\lambda}$ ):

$$\sigma_{abs,BrC,\lambda} = \sigma_{abs,\lambda} - \sigma_{abs,BC,\lambda} \quad (7)$$

227 The light absorption data at 880 nm ( $\sigma_{abs,880nm}$ ) were selected to represent BC absorption  
228 ( $\sigma_{abs,BC,880nm}$ ), which shall not be affected by BrC (Drinovec et al., 2015). It has been reported  
229 that the dust-related contributions of PM<sub>2.5</sub> were normally less than 5% in wintertime in  
230 Guangzhou; therefore, the influence from dust could be negligible in this study (Huang et al.,  
231 2014).

### 232 2.2.3 Estimation of AAE<sub>BC</sub>

233 Traditionally, AAE<sub>BC</sub> was believed to be close to 1.0 (Bodhaine, 1995), which has been  
234 commonly used for BC measurements (Olson et al., 2015). However, studies have  
235 demonstrated that AAE<sub>BC</sub> can be affected by the refractive index of coating materials, mixing  
236 state, morphology, and BC core size (Liu et al., 2015). Therefore, using the default AAE<sub>BC</sub> = 1  
237 may lead to uncertainty in BrC absorption estimation. To obtain the correct AAE<sub>BC</sub>, a series of  
238 Mie theory calculations were conducted using a simplified core-shell model (Bohren and  
239 Huffman, 1983; Wang et al., 2018). We used a modified BHCOAT code and BHMIE code to  
240 calculate the aerosol optical properties of the core-shell and external mixture at different  
241 wavelengths (Cheng et al., 2006). In the Mie theory, a particle is taken as a perfect  
242 homogeneous sphere, and its extinction and scattering efficiencies,  $Q_{ext,Mie,\lambda}$  and  $Q_{scat,Mie,\lambda}$ ,  
243 respectively, are expressed as (Mie, 1908; Seinfeld and Pandis, 1998):

$$Q_{ext,Mie,\lambda} = \frac{2}{\alpha^2} \sum_{n=1}^{\infty} [(2n+1)Re(a_n + b_n)] \quad (8)$$

$$Q_{scat,Mie,\lambda} = \frac{2}{\alpha^2} \sum_{n=1}^{\infty} [(2n+1)(|a_n|^2 + |b_n|^2)] \quad (9)$$

246 where  $\alpha = \pi D_p/\lambda$  is the size parameter;  $a_n$  and  $b_n$  are functions of the complex refractive  
247 index (RI) and  $\alpha$  in the Riccati-Bessel form, respectively.  $Re$  in Eq. (8) denotes that only the  
248 real part of RI is taken. The absorption efficiency ( $Q_{abs,Mie,\lambda}$ ) is thus the difference between  
249 the extinction and scattering efficiencies:

$$Q_{abs,Mie,\lambda} = Q_{ext,Mie,\lambda} - Q_{scat,Mie,\lambda} \quad (10)$$

Then, the absorption coefficient  $\sigma_{abs,Mie,\lambda}$  was obtained by the following (Bricaud and Morel, 1986):

$$\sigma_{abs,Mie,\lambda} = \int Q_{abs,Mie,\lambda} \cdot \left(\frac{\pi}{4} D_p^2\right) \cdot N(\log D_p) \cdot d \log D_p \quad (11)$$

where  $N(\log D_p)$  is the PNSD function. A two-component parameterization of dry particles, i.e., the BC core and the nonlight-absorbing species, was applied to calculate aerosol optical properties here (Wex et al., 2002).  $\tilde{m}_{core}$  represents the RI of the BC core, and  $\tilde{m}_{non}$  represents the RI of nonlight-absorbing particles.

In a realistic atmosphere, some nonlight-absorbing particles may exist independently without BC (Liu et al., 2013; Cheung et al., 2016). In this work, the portion of nonlight-absorbing particles at a certain size ( $D_p$ ) was determined by our previous measurements at the same site using a Volatility Tandem Differential Mobility Analyzer (V-TDMA), during which completely vaporized (CV) particles at 300°C were referred to as nonlight-absorbing particles that externally mixed with other BC-containing particles. Thus, the PNSD of CV particles ( $N(\log D_p)_{CV}$ ) and BC-containing particles ( $N(\log D_p)_{BC}$ ) can be given by the following equations:

$$N(\log D_p)_{CV} = N(\log D_p)_{measure} \cdot \Phi(D_p)_{N,CV} \quad (12)$$

$$N(\log D_p)_{BC} = N(\log D_p)_{measure} \cdot (1 - \Phi(D_p)_{N,CV}) \quad (13)$$

where  $N(\log D_p)_{measure}$  is the PNSD of the measured particles from SMPS and APS.  $\Phi(D_p)_{N,CV}$  was the number fraction of CV particles in different size bin.

A previous study applied three kinds of BC mixture models to calculate the aerosol optical properties, including external, homogeneously internal and core-shell mixtures (Bohren and Huffman, 2007; Seinfeld and Pandis, 1998). To quantify the mixing state of BC,  $r_{ext}$  was defined as the mass fraction of externally mixed BC ( $M_{ext}$ ) in total BC ( $M_{BC}$ ):

$$r_{ext} = \frac{M_{ext}}{M_{BC}} \quad (14)$$

Tan et al. (2016) suggested that two extreme conditions of external and core-shell mixtures comprised the actual mixing state of BC in the PRD. Hence, we simply divided the PNSD of BC into the PNSD from an external mixture of BC and a core-shell mixture of BC. The PNSDs

278 of externally mixed BC particles and core-shell mixed BC particles were referred to by the  
 279 following equations with a given  $r_{ext}$ .

$$280 \quad N(\log D_p)_{ext} = N(\log D_p)_{BC} \cdot f_{BC} \cdot r_{ext} \quad (15)$$

$$281 \quad N(\log D_p)_{core-shell} = N(\log D_p)_{BC} \cdot (1 - f_{BC} \cdot r_{ext}) \quad (16)$$

282  $f_{BC}$  was defined as the BC volume fraction in the BC-containing particle volume, which can be  
 283 converted from the BC mass concentration:

$$284 \quad f_{BC} = \frac{M_{BC}}{\rho_{BC} \cdot \sum D_p N(\log D_p)_{BC} \cdot \left(\frac{\pi}{6} D_p^3\right)} \quad (17)$$

285 where  $\rho_{BC}$  is the density of BC and is assumed to be  $1.5 \text{ g cm}^{-3}$  (Ma et al., 2012);  $M_{BC}$  is the BC  
 286 mass concentration derived from the multi-angle absorption photometer (MAAP), which was  
 287 obtained by an empirical formula from the Aethalometer that measured the BC concentration  
 288 ( $M_{BC,AE}$ ), as proposed by Wu et al. (2009):

$$289 \quad M_{BC} = 0.897 \cdot M_{BC,AE} - 0.062 \quad (18)$$

290 The PNSDs of externally mixed nonlight-absorbing particles and externally mixed BC particles  
 291 were input into the BHMIE code, and the PNSD of the core-shell mixed particles was imported  
 292 into the BHCOAT code. Another critical parameter for the core-shell model was the diameter  
 293 of the BC core. For the simplified core-shell model we applied, the visualization was that a  
 294 homogeneous BC core sphere was encapsulated in a shell of non-absorbing coating (Bohren  
 295 and Huffman, 2007). Without size-resolved coating thickness measurements, core-shell mixed  
 296 particles simply assumed that cores with the same diameter had the same coating thickness.  
 297 Therefore, the diameter of the BC core was calculated as follows:

$$298 \quad D_{core} = D_p \cdot \left( \frac{f_{BC} - f_{BC} \cdot r_{ext}}{1 - f_{BC} \cdot r_{ext}} \right)^{\frac{1}{3}} \quad (19)$$

299  $D_{core}$  and  $D_p$  are inputted as parameters into  $a_n$  and  $b_n$ , respectively, which was described by  
 300 Bohren and Huffman (2007). [The corresponding time series of size distribution of the derived](#)  
 301 [external BC and internal BC core were illustrated in Fig. S2.](#) Thus, the  $\sigma_{abs,BC,Mie, \lambda_i}$  values of  
 302 all six wavelengths were calculated through the Mie model, and then the  $AAE_{BC}$  values of those  
 303 five wavelengths were obtained using Eq. (6). The performance of this empirically determined  
 304 calculation method has been compared with other possible BC mixing schemes in details (see  
 305 Table 1).

#### 306 2.2.4 Atmospheric radiative transfer model

307 In this work, the Santa Barbara DISORT Atmospheric Radiative Transfer (SBDART) model  
 308 was employed to estimate the DRF of BrC absorption, i.e., its effects on the downward and  
 309 upward fluxes ( $F$  in  $\text{W m}^{-2}$ ) of solar radiation at the TOA. SBDART is a software tool that can  
 310 be used to compute plane-parallel radiative transfer under both clear and cloudy conditions  
 311 within the atmosphere. More details about this model have been described by Ricchiazzi et al.  
 312 (1998). Both ground measurements and remote sensing data were used in the simulation. The  
 313 surface albedo was derived from a 500 m resolution MODIS BRDF/albedo model parameter  
 314 product (MCD43A3, daily). The MCD43A3 products are the total shortwave broadband black-  
 315 sky albedo ( $\alpha_{BSA}$ ) and white-sky albedo ( $\alpha_{WSA}$ ), while the actual surface albedo ( $\alpha$ ) was  
 316 computed from a linear combination of  $\alpha_{WSA}$  and  $\alpha_{BSA}$ , which were weighted by the diffuse ratio  
 317 ( $r_d$ ) and direct ratio ( $1-r_d$ ), respectively:

$$318 \quad \alpha = (1 - r_d) \cdot \alpha_{BSA} + r_d \cdot \alpha_{WSA} \quad (20)$$

319  $r_d$  was obtained from an exponential fit of Eq. (21) based on empirical observations (Stokes and  
 320 Schwartz, 1994; Roesch, 2004):

$$321 \quad r_d = 0.122 + 0.85 e^{-4.8\mu_0} \quad (21)$$

322 where  $\mu_0$  is the cosine of the zenith angle, which is calculated by the model for any specified  
 323 date, time, and latitude and longitude of the site. The surface-based aerosol optical properties,  
 324 including the aerosol light absorption coefficients of both BC and BrC, i.e., differentiated from  
 325 each other under the assumption of uniform AAE<sub>BC</sub>, along with the nephelometer-measured  
 326 aerosol scattering coefficients, were used to calculate the SSA at different wavelengths  
 327 according to Eq. (22),

$$328 \quad SSA(\lambda) = \frac{\sigma_{scat, \lambda}}{\sigma_{abs, BrC, \lambda} + \sigma_{abs, BC, \lambda} + \sigma_{scat, \lambda}} \quad (22)$$

329 which was then used in the model calculation. Finally, the AOD and asymmetry factor (ASY)  
 330 at 440, 675 and 870 nm were derived from the Aerosol Robotic Network (AERONET)  
 331 measurements at the Hong Kong Polytechnic University site (Holben et al., 1998), which is  
 332 approximately 115 km to the southeast of the Panyu site. The tropical atmospheric profile was  
 333 used in the SBDART model based on the prevailing weather conditions in the PRD. The aerosol  
 334 DRF ( $\Delta F$ ) was calculated as the difference between the downward and upward radiation fluxes:

$$335 \quad \Delta F = F \downarrow - F \uparrow \quad (23)$$

### 336 3 Results and discussion

#### 337 3.1 Aerosol light absorption

338 The  $AAE_{BC}$  is widely defined as the uniform representation of the wavelength dependence of a  
339 BC particle (Olson et al., 2015). In reality,  $AAE_{BC}$  may vary significantly with BC containing  
340 aerosols of different sizes, mixing states, and morphologies (Scarnato et al., 2013; Lack and  
341 Langridge, 2013). In fact, some studies showed that the AAE of a large-size, pure BC core may  
342 be less than 1.0 (Liu et al., 2018) and that the AAE of BC coated with a non-absorbing shell  
343 may be larger than that under uniformity (Lack and Cappa, 2010).

344 It has been suggested that a significant fraction of smaller size particles is non BC-containing  
345 (Ma et al., 2017; Cheung et al., 2016). BC and non-BC materials can also be externally or  
346 internally mixed. Although size resolved BC measurements were not available during this work,  
347 we have conducted size resolved Volatility Tandem Differential Mobility Analyzer (V-TDMA)  
348 measurements at 300°C for 40, 80, 110, 150, 200 and 300 nm, respectively, during an earlier  
349 field campaign (February 2014) at the same site as in this work. At 300°C, all non-BC particle  
350 will be completely vaporized (CV) and thus the portion of non BC particles at such size, denoted  
351 as  $\Phi_{N,CV}$ , can be determined. [The average  \$\Phi\_{N,CV}\$  values were 0.384, 0.181, 0.180, 0.158, 0.143](#)  
352 [and 0.137, corresponding to 40, 80, 110, 150, 200 and 300 nm \(see Fig. S3\), respectively](#)  
353 [\(Cheung et al., 2016; Tan et al., 2016a\). The size-independent  \$\Phi\_{N,CV}\$  was interpolated linearly](#)  
354 [with these six diameters. For particle size larger than 300 nm and less than 40 nm,  \$\Phi\_{N,CV}\$  values](#)  
355 [were set to 0.137 and 0.384, respectively.](#) For particle size larger than 300 nm and less than 40  
356 nm,  $\Phi_{N,CV}$  values were set to 0.137 and 0.384, respectively. Accordingly, the complete  
357 distribution of  $\Phi_{N,CV}$  for the whole PNSD was obtained. The mixing states of BC particles were  
358 also estimated here, i.e., the mass portion of externally mixed BC with respect to total BC,  
359 denoted as  $r_{ext}$ . The value of  $r_{ext}$  was taken as 0.58, which was obtained using an optical closure  
360 method during a previous field experiment at this site (Tan et al., 2016a). During the following  
361 Mie theory calculation, a fixed refractive index ( $\tilde{m}_{core}=1.80-0.54i$ ,  $\tilde{m}_{non}=1.55-10^{-7}i$ ) was  
362 adopted for the whole size range. Accordingly, the calculated BC absorption at 880 nm ( $Abs_{880}$ )  
363 was  $21.869 \text{ Mm}^{-1}$ , which is reasonably close to the measured mean value of  $21.199 \text{ Mm}^{-1}$ . To  
364 further validate our calculation scheme (Base Case), we have considered several extreme cases.  
365 Case 1: BC is completely externally mixed with non-BC particles, i.e.,  $\Phi_{N,CV} = 0$  and  $r_{ext} = 1$ ;

366 Case 2: BC is present in every size bin and BC is completely internally mixed with non-BC  
367 material, i.e.,  $\Phi_{N,CV} = 0$  and  $r_{ext} = 0$ ; Case 3: BC is both internally and externally mixed but there  
368 is no non-BC-containing particles, i.e.,  $\Phi_{N,CV} = 0$  and  $r_{ext} = 0.58$ ; Case 4: BC is internally mixed  
369 with non-BC material and there is non-BC particles present, i.e.,  $\Phi_{N,CV}$  ranges from 0.384 to  
370 0.137 and  $r_{ext} = 0$ ; Case 5: the same as case 4 except assuming a fixed non-BC to BC ratio of  
371 0.5, i.e.,  $\Phi_{N,CV} = 0.5$ ,  $r_{ext} = 0$ ; Case 6: the same as case 5 except that some externally mixed BC  
372 is also present, i.e.,  $\Phi_{N,CV} = 0.5$ ,  $r_{ext} = 0.58$ . The calculation results are listed in Table 1. Evidently,  
373 case 1 (complete externally mixed) will significantly underestimate the measured  $Abs_{880}$ ,  
374 indicating that most BC particles were not likely externally mixed at the Panyu site. Complete  
375 internal mixing state (case 2, 4, and 5), on the contrary, would substantially overestimate the  
376 BC absorption regardless the form of BC core distribution function. However, when the  $r_{ext}$   
377 were considered (case base, 3, and 6), the calculated  $Abs_{880}$  values were all very close to the  
378 measured value.

379 When the  $AAE_{BC}$  was assumed to be uniform, the campaign-averaged  $\sigma_{BrC}$  values were  
380  $17.6 \pm 13.7 \text{ Mm}^{-1}$  at 370 nm,  $9.7 \pm 7.9 \text{ Mm}^{-1}$  at 470 nm,  $5.8 \pm 5.1 \text{ Mm}^{-1}$  at 520 nm,  $4.0 \pm 3.5 \text{ Mm}^{-1}$  at  
381 590 nm and  $2.3 \pm 2.1 \text{ Mm}^{-1}$  at 660 nm. At the corresponding wavelengths, BrC absorption  
382 contributed  $26.2 \pm 8.5\%$ ,  $20.0 \pm 7.3\%$ ,  $14.3 \pm 6.5\%$ ,  $11.7 \pm 5.3\%$ , and  $7.8 \pm 4.1\%$  to the total aerosol  
383 absorption, respectively. When the  $AAE_{BC}$  was applied as the result of the Mie model  
384 calculation, the corrected campaign-averaged  $\sigma_{abs,BrC}$  values were  $23.5 \pm 17.7 \text{ Mm}^{-1}$  at 370 nm,  
385  $11.8 \pm 9.5 \text{ Mm}^{-1}$  at 470 nm,  $6.7 \pm 5.7 \text{ Mm}^{-1}$  at 520 nm,  $4.6 \pm 3.9 \text{ Mm}^{-1}$  at 590 nm and  $2.6 \pm 2.3 \text{ Mm}^{-1}$   
386 at 660 nm. At the corresponding wavelengths, BrC absorption contributed  $34.1 \pm 8.0\%$ ,  
387  $23.7 \pm 7.3\%$ ,  $16.0 \pm 6.7\%$ ,  $13.0 \pm 5.4\%$ , and  $8.7 \pm 4.3\%$  to the total aerosol absorption (see Fig. 2),  
388 respectively. Evidently, aerosol light absorption was predominantly due to BC; however, BrC  
389 also played a significant role, especially at shorter wavelengths. Table 2 shows the  
390 intercomparison of BrC light absorption in the near UV range between this work and other  
391 studies in the East Asian region. Clearly, the reported values vary substantially, and our result  
392 is toward the lower end of values. [Figure. S4 displayed the time series of particle AAE](#)  
393 [measured by the Aethalometer and  \$AAE\_{BC}\$  was derived from Mie model calculation. The](#)  
394 [AAE<sub>BC</sub> was almost always lower than AAE, indicating appreciable BrC light absorption at the](#)  
395 [Panyu site.](#)

396 **3.2 Uncertainty in BC and BrC optical differentiation**

397 Theoretically, the magnitude of BC absorptions can be affected by both parts of the complex  
398 refractive indexes (RIs); thus,  $AAE_{BC}$  may also vary with the RIs of both the BC core and  
399 coating shell. In fact, RI was also one of the least known properties of BC and other coating  
400 materials with negligible absorbing capabilities. The refractive index of the BC core ( $\tilde{m}_{core}$ )  
401 displays a wide range of variations (Liu et al., 2018). Typically, the real and imaginary parts of  
402 the RI can vary from 1.5 to 2.0 and 0.5 to 1.1, respectively. In addition, the shell was assumed  
403 to consist of non-absorbing material in the core-shell model, i.e., its imaginary RI was set to be  
404 close to zero ( $10^{-7}$ ). The real part of the non-absorbing material RI ( $\tilde{m}_{non}$ ) may vary from 1.35  
405 to 1.6 due to the presence of OA (Zhang et al., 2018; Redmond and Thompson, 2011) and  
406 inorganic salts (Erlick et al., 2011). Hence, it is necessary to investigate the uncertainties  
407 associated with the variations in  $AAE_{BC}$  by varying the RIs of both the BC core and the non-  
408 absorbing materials.

409 Figure 3 shows the impacts of RI on the evaluations of  $AAE_{BC}$  based on core-shell and external  
410 configuration, where the RI of the BC core was set to be constant, i.e.,  $\tilde{m}_{core}=1.80-0.54i$ , and  
411 the real part of  $\tilde{m}_{non}$  varied from 1.35 to 1.6 at an interval of 0.05, with the imaginary part of  
412  $\tilde{m}_{non}$  set at  $10^{-7}$ . As shown in Fig. 3a, the calculated  $AAE_{BC}$  for the core-shell model was higher  
413 than 1.0 at longer wavelengths (520 to 880 nm) and lower than 1.0 at shorter wavelengths (370  
414 to 520 nm) (the red line in Fig. 3 denotes  $AAE_{BC}=1$ ). The averaged  $AAE_{BC,370-520nm}$  ranged from  
415 0.84 to 0.87, and the  $AAE_{BC,520-880nm}$  ranged from 1.07 to 1.15, indicating that the  $AAE_{BC,520-}$   
416  $880nm$  appeared to be more sensitive to the shell's real part than  $AAE_{BC,370-520nm}$ . Even if the shell  
417 material was assumed to be non-absorbing, the variation in the real RI of the shell, which was  
418 referred to as the real part of  $\tilde{m}_{non}$ , still led to changes in the shell's refractivity and  
419 correspondingly altered its lensing effect, causing a change in  $AAE_{BC}$ . Meanwhile,  $AAE_{BC,370-}$   
420  $520nm}$  and  $AAE_{BC,520-880nm}$  generally increased with an increasing real part of the shell. In Fig. 3b,  
421 under the externally mixed conditions,  $AAE_{BC,370-520nm}$  and  $AAE_{BC,520-880nm}$  were both less than  
422 1.0. The average  $AAE_{BC,370-520nm}$  was 0.33, and the average  $AAE_{BC,520-880nm}$  was 0.63. These  
423 values were far less than the values under core-shell mixture conditions. In the external mixture  
424 model, the BC core and nonlight-absorbing materials were assumed to exist dependently, and  
425 then the optical properties of these two components were considered separately. Therefore,

426 altering the real part of the externally mixed non-absorbing material would not affect the light  
427 absorption property of the BC core or  $AAE_{BC}$ .

428 The impacts of the BC core on  $AAE_{BC}$  are shown in Fig. 4, where the refractive index of  
429 nonlight-absorbing materials was assumed to be  $\tilde{m}_{non}=1.55-10^{-7}i$  and  $\tilde{m}_{non}$  was wavelength-  
430 independent. Fig. 4 was obtained with a core-shell mixture model (Fig. 4a and 4b) and an  
431 external mixture model (Fig. 4c and 4d) by varying the real part of  $\tilde{m}_{core}$  from 1.5 to 2.0 with  
432 a step of 0.05 and varying the imaginary part of the  $\tilde{m}_{core}$  from 0.4 to 1.0 with a step of 0.05,  
433 respectively. As shown in Figs. 4a and 4b, for the core-shell mixture, the averaged  $AAE_{BC,370-}$   
434  $520nm$  ranged from 0.55 to 0.99, and the averaged  $AAE_{BC,520-880nm}$  ranged from 0.84 to 1.27. The  
435  $AAE_{BC}$  at a certain wavelength generally increased when increasing the real part of  $\tilde{m}_{core}$  but  
436 decreased when increasing the imaginary part of  $\tilde{m}_{core}$ . The  $AAE_{BC}$  appeared to be more  
437 sensitive to the imaginary part of  $\tilde{m}_{core}$  than the real part of  $\tilde{m}_{core}$  because the imaginary part  
438 of  $\tilde{m}_{core}$  was directly related to the light-absorbing properties of particles. In Fig. 4c and 4d,  
439 for the external mixture, the averaged  $AAE_{BC,370-520nm}$  ranged from 0.04 to 0.45 and the averaged  
440  $AAE_{BC,520-880nm}$  ranged from 0.28 to 0.79, while the averaged  $AAE_{BC,370-520nm}$  and  $AAE_{BC,520-}$   
441  $880nm$  were both less than 1.0. Similar to the core-shell mixture, the  $AAE_{BC,520-880nm}$  increased  
442 when increasing the real part of  $\tilde{m}_{core}$  but decreased when increasing the imaginary part of  
443  $\tilde{m}_{core}$ . However, the variation patterns of  $AAE_{BC,370-520nm}$  were different from those of  $AAE_{BC,520-}$   
444  $880nm$ . The  $AAE_{BC,370-520nm}$  values were not changed by altering the real part of  $\tilde{m}_{core}$  within the  
445 low imaginary part of  $\tilde{m}_{core}$ , whereas the  $AAE_{BC,370-520nm}$  values still increased when increasing  
446 the real part of  $\tilde{m}_{core}$  within the high imaginary part of  $\tilde{m}_{core}$ . A possible explanation was that  
447 the externally mixed BC core had weak light absorption within the low imaginary part of  $\tilde{m}_{core}$ ,  
448 causing the  $AAE_{BC,370-520nm}$  values to be insensitive to the real part of  $\tilde{m}_{core}$ . The  $AAE_{BC,520-880nm}$   
449 values were higher than the  $AAE_{BC,370-520nm}$  values regardless of whether in they were for the  
450 core-shell mixture or external mixture. In addition, the  $AAE_{BC}$  values conducted by the core-  
451 shell mixture were higher than those conducted by the external mixture.

452 Figure 4 demonstrates that the variation in the imaginary RI of the BC core has the most  
453 significant impact on the estimated  $AAE_{BC}$ , indicating that the chemical component of BC  
454 emitted from different sources leads to a large uncertainty in  $AAE_{BC}$  estimation. At the same  
455 time, the influence arising from varying the real RI of the BC core was relatively moderate.

456 Nevertheless, Fig. 3 demonstrated that change in the real RI of the non-absorbing materials  
457 caused the least/no impact compared to that caused by the variations in the complex RI of the  
458 BC core.

459 It should be pointed out that most BC-containing particles are often observed as fractal rather  
460 than spherical in shape (Katrinak et al., 1993). Because the Mie model assumes that all particles  
461 are spherical, it may lead to potential uncertainty for the estimation of  $AAE_{BC}$  and BrC  
462 absorption contributions. Moreover, the externally mixed soot aggregates were “chain-like” or  
463 “puff-like” in the PRD dry season (Feng et al., 2010), in which the fractal dimension ( $D_f$ ) was  
464 between 1.5 and 2.0. Coating soot aggregates were likely sphere ( $D_f$  approaches 3) from the  
465 high-resolution transmission electron microscopy (TEM) measurements taken in Hongkong  
466 ((Zhou et al., 2014)). A soot aggregate sensitivity study with the superposition T-matrix method  
467 indicated that using the assumption of volume-equivalent spheres for the soot aggregates may  
468 result in an overestimation of approximately up to 15% and an underestimation of  
469 approximately up to 50% in the predicted 870 nm light absorption when the  $D_f$  is between 1.5  
470 and 3.0 (Liu et al., 2008). However, it should be recognized that the complex shapes or positions  
471 of the BC core inside the particle make it impractical to be numerically simulated in the exact  
472 details. By far the Mie model with a core-shell configuration would be the most practical and  
473 effective simulation scheme for BC particle optical property simulation.

474 Furthermore, we have performed Monte Carlo simulations to evaluate the uncertainties of the  
475 Mie calculation performed during this work. In the simulation, a sequence of random numbers  
476 or errors were applied to the input parameters, and then the corresponding uncertainties of  
477 particle light absorption and  $AAE_{BC}$  by were computed using the Mie model. Five hundred of  
478 reiteration were conducted during the simulation such that the random errors will be normally  
479 distributed. The standard deviations ( $\sigma$ ) of all input parameters are listed in Table S1. In order  
480 to cover the effect of extreme value, we used a range of  $\pm 3\sigma$ , or a confidence level of 99%, in  
481 the Monte Carlo simulation. Table S2 listed the Monte Carlo simulation results, i.e., the average  
482 relative standard deviations ( $\sigma_{Mie}$ ) of the calculated BC light absorption at 880 nm ( $Abs_{880}$ ),  
483  $AAE_{BC,370-520}$ , and  $AAE_{BC,520-880}$ . The uncertainties of the calculated  $Abs_{880}$ ,  $AAE_{BC,370-520}$ , and  
484  $AAE_{BC,520-880}$  at 2 times of  $\sigma_{Mie}$ , i.e., at a confidence coefficient of 95%, were approximately  
485  $\pm 31\%$ ,  $\pm 16\%$ , and  $\pm 13\%$ , respectively. Figure S5 also showed the time series of the uncertainties

**Deleted:** We want to...t should be note ...ointed out that most BC-containing particles are often observed as fractal rather than spherical in shape (Katrinak et al., 1993). Because the Mie model assumes that all particles are spherical, it may lead to potential uncertainty for the estimation of  $AAE_{BC}$  and BrC absorption contributions. Moreover, the externally mixed soot aggregates were “chain-like” or “puff-like” in the PRD dry season (Feng et al., 2010), in which the fractal dimension ( $D_f$ ) was between 1.5 and 2.0. Coating soot aggregates were likely sphere ( $D_f$  approaches 3) from the high-resolution transmission electron microscopy (TEM) measurements taken in Hongkong ((Zhou et al., 2014)). A soot aggregate sensitivity study with the superposition T-matrix method indicated that using the assumption of volume-equivalent spheres for the soot aggregates may result in an overestimation of approximately up to 15% and an underestimation of approximately up to 50% in the predicted 870 nm light absorption when the  $D_f$  is between 1.5 and 3.0 (Liu et al., 2008). However, itwe...should be recognized the fact ...hat different ...he complex shapes or positions of the BC core inside the particle positions may...ake it impractical to be bring more difficult computational problems in practical ...umerically simulations...imulated in the exact details. By far Applying ...he simplified ...ie model with a core-shell configuration would be a ...he most practical and effective simulation scheme tradeoff scheme without...or BC particle optical property simulation. particulate material morphological measurements in Panyu. (... [1])

**Deleted:** acquire ...he uncertainties of the Mie calculation performed during this work. In the Monte Carlo ...imulation, a applied ...equences...of random numbers or errors were applied to vary ...he input parameters, and then,...we (... [2])

**Deleted:** running the repeated...omputed using the Mie calculationmodel. (Yuan et al., 2016b). 500...ive hundred of reiteration were conducted during the simulation such that the random errors will be normally distributedtrials of the calculation are adequate to random the input parameters according to the normal distribution... The input parameters normally distributed around the desired value with (... [3])

**Formatted:** Subscript

**Formatted:** Font color: Text 1

**Deleted:** possible values for the input parameters... Th (... [4])

**Formatted** (... [5])

575 [of  \$Abs\_{880}\$ ,  \$AAE\_{BC,370-520}\$  and  \$AAE\_{BC,520-880}\$  from Monte Carlo simulation for the campaign period.](#)

### 576 **3.3 Characteristics of BrC light absorption, water-soluble ions and OC concentrations**

577 Globally, BrC has been observed to be highly correlated with biomass and biofuel burning  
578 emissions (Laskin et al., 2015). Since large quantities of sylvite are present in biomass burning  
579 particles, the  $K^+$  abundance has often been used as a biomass burning tracer (Levine, 1991).  
580 Figure 5 presents the time series of the OC mass concentration,  $K^+$  concentration, and BrC  
581 absorption from 29 November 2014 to 2 January 2015 at the Panyu site. The range of the OC  
582 concentration obtained from the OC/EC online analyzer was from 1.5 to 65.2  $\mu\text{g cm}^{-3}$  and the  
583 campaign average was  $12.5 \pm 7.3 \mu\text{g cm}^{-3}$ . The BrC absorption hourly mean data were between  
584 0.2 and 123.2  $\text{Mm}^{-1}$  and the campaign average was  $23.5 \pm 17.7 \text{Mm}^{-1}$ . On the other hand, the  
585 average  $K^+$  concentration was  $1.0 \pm 0.7 \mu\text{g cm}^{-3}$  (ranging from 0 to 5.4  $\mu\text{g cm}^{-3}$ ). Clearly, similar  
586 trends among OC,  $K^+$ , and BrC absorption can be seen during this field campaign (Fig. 5).

587 To investigate the origins of these observed OC,  $K^+$ , and BrC, wind rose plots (as shown in Fig.  
588 6) were generated for OC,  $K^+$ , and BrC absorption, respectively. All three panels of Fig. 6  
589 consistently show that the three substances were associated with the same wind pattern. For the  
590 entire campaign period, the highest values of OC,  $K^+$ , and  $\sigma_{abs,BrC,370nm}$  were mostly associated  
591 with southwesterly winds with a relatively low wind speed ( $\sim 2 \text{ m s}^{-1}$ ). The relatively higher OC  
592 and  $K^+$  concentrations were highly related to the seasonal straw burning in the countryside of  
593 the PRD located to the west of the Panyu station. In contrast, OC and  $K^+$  concentrations during  
594 periods with easterly winds were substantially lower than those during periods with westerly  
595 winds. The wind rose plot of  $\sigma_{abs,BrC,370nm}$  is shown in Fig. 6c. Similar to OC and  $K^+$ ,  $\sigma_{abs,BrC,370nm}$   
596 showed higher values under weak ( $< 2 \text{ m s}^{-1}$ ) westerly winds and lower values from the north  
597 and south, indicating that BrC absorption was likely attributed to local sources and was  
598 accumulated under calm wind conditions. [Figure S6 showed the 3-day backward trajectory and](#)  
599 [the fire counts for 5 to 7 \(Fig. S6a\), 12 to 14 \(Fig. S6b\) and 24 to 26 \(Fig. S6c\) in November](#)  
600 [2014, representing low loading, moderate loading and high loading period. Clearly, the high](#)  
601 [loading period concurred with stagnant air movement and higher fire counts, indicating the](#)  
602 [contribution from open fire burning sources.](#) However, there was a detectable difference among  
603 the three rose plots [of Fig. 6](#) in the maximum concentration direction. A possible explanation  
604 was that although biomass burning emissions were believed to be the dominant and primary

605 source of OC,  $K^+$ , and BrC, their emission ratios were highly variable and may change with the  
606 type of biofuel and burning condition and may even vary during different stages of burning  
607 (Burling et al., 2012). Although biomass burning emissions contain substantial light-absorbing  
608 BrC, further atmospheric aging processes may significantly reduce its light-absorbing  
609 capability (Satish et al., 2017). Moreover, secondary formation may also lead to BrC formation  
610 inside these primary aerosols, such as humic-like substances formed through aqueous-phase  
611 reactions, which have been suggested to be an important component of BrC (Andreae and  
612 Gelencser, 2006).

613 To further explore the possible sources of BrC optical absorption, the diurnal variations in OC,  
614  $K^+$ ,  $\sigma_{abs,BrC,370nm}$ , and  $\sigma_{abs,BrC,370nm}/OC$  values are plotted in Fig. 7. The diurnal variation in OC  
615 at the Panyu site appeared to be dominated by the development of the planetary boundary layer  
616 (PBL) height, i.e., primary emissions accumulated at night and were swiftly diluted by vertical  
617 mixing in the morning. The slight increase in OC in the afternoon indicated that photochemistry  
618 may have still weakly contributed to SOA formation. [Fig. 7b](#) shows the diurnal variation in  $K^+$ .

619 Unlike OC,  $K^+$  shows a small peak at approximately 6 AM, which was consistent with breakfast  
620 time and was very likely due to cooking activities using biofuel. No lunch and dinner time  $K^+$   
621 peaks were observed. The most likely explanation is that the boundary layer height is much  
622 higher during lunch and dinner time than in the early morning, providing a much better  
623 atmospheric diffusion condition for air pollutants. It is still a common practice to collect straw  
624 as biofuel in local rural areas, which can be visually spotted but is not heavily utilized in the  
625 region. However, the diurnal profile of  $\sigma_{abs,BrC,370nm}$  (see Fig. 7c) shows the combined features  
626 of OC and  $K^+$  since both primary and secondary processes affect its intensity. The nighttime  
627 increasing trend was most likely attributed to straw burning activities in early winter in nearby  
628 rural areas that continued to accumulate within the shallow PBL (Jiang et al., 2013).  
629  $\sigma_{abs,BrC,370nm}/OC$ , i.e., the mass absorption coefficient of BrC ( $MAC_{BrC}$ ) (Fig. 7d), showed a  
630 relatively flat pattern, with a pronounced dip in the afternoon and higher values at nighttime,  
631 which was likely due to enhanced primary emissions and stable stratification at nighttime.  
632 Declining trends during the late morning and afternoon hours indicated that the aging process  
633 and photochemical production may reduce the light-absorbing capacity of BrC (Qin et al.,  
634 2018).

Deleted: Figure

636 Furthermore, Fig. 8 shows the linear regression analysis results used to evaluate the correlations  
637 of  $\sigma_{abs,BrC,370nm}$  with the OC,  $K^+$ ,  $Ca^{2+}$ ,  $Mg^{2+}$ , Cl,  $SO_4^{2-}$ ,  $NO_3^-$ , and  $NH_4^+$  concentrations. The best  
638 correlations can be found between  $\sigma_{abs,BrC,370nm}$  and  $K^+$  ( $R^2=0.6148$ ), followed by those between  
639  $\sigma_{abs,BrC,370nm}$  and OC ( $R^2=0.4514$ ),  $NO_3^-$  ( $R^2=0.4224$ ) and  $NH_4^+$  ( $R^2=0.4656$ ). Source  
640 apportionment analysis of OA and BrC absorption in Beijing and Guangzhou illustrated that  
641 biomass burning organic aerosols (BBOAs) correlated well with BrC light absorption (Xie et  
642 al., 2018; Qin et al., 2018). Thus, the significant correlation between BrC absorption and  $K^+$   
643 reaffirmed that biomass burning was the crucial emission source of BrC observed in this work.  
644 Although the geographic location of the observation site was situated in a coastal area and  $K^+$   
645 could also be found in sea salt (Pio et al., 2008), it should be noted that the prevailing wind  
646 direction during winter was from the north (see Fig. 3), which drives maritime air parcels away  
647 from the site. Hence, the effect of sea salt and crustal materials to  $K^+$  was slight, which was  
648 demonstrated in the supplementary information as shown in Fig. S8. Other earlier studies also  
649 suggested that the sea salt contribution to the  $K^+$  concentrations of  $PM_{2.5}$  was trivial in the PRD  
650 region during the winter (Lai et al., 2007). Another possible  $K^+$  source was coal combustion.  
651 The coal consumption in the PRD region was dominated by coal-fired power plants. The  
652 emission from power plants was usually very steady and was less likely to affect the diurnal  
653 correlation between  $K^+$  and BrC absorption. As shown in Fig. S7, the ratios of  $K^+/PM_{2.5}$  varies  
654 approximately from 0.015 and 0.020 and the diurnal profile of  $K^+/PM_{2.5}$  shows very little  
655 variation. Yu et al. (2018) have suggested that  $K^+$  usually accounted for 2.34-5.49% of  $PM_{2.5}$  in  
656 the laboratory biomass burning study. However,  $K^+$  was normally lower than 1% of coal  
657 combustion  $PM_{2.5}$ . Therefore, the ratio range of  $K^+$  to  $PM_{2.5}$  observed in this work likely  
658 indicated aged biomass burning particles. Both nitrogen oxides ( $NO_x$ ) and ammonia ( $NH_3$ ) can  
659 be found in biomass burning plumes (Andreae and Merlet, 2001). For  $NO_3^-$  and  $NH_4^+$ , nitrate  
660 can be converted from  $NO_x$  through atmospheric reactions, and ammonium may originate from  
661  $NH_3$ . However, similar to the diurnal variation in  $\sigma_{abs,BrC,370nm}$ , diurnal variations in  $NH_4^+$  and  
662  $NO_3^-$  also increased in the afternoon and appeared at nighttime in Fig S7. However,  $NO_3^-/PM_{2.5}$   
663 and  $NH_4^+/PM_{2.5}$  reached their peaks at noon, indicating that ammonium nitrate formed from the  
664 secondary reaction at this time. Along with the reduced boundary layer height and ambient  
665 temperature,  $NO_3^-$  was accumulated until the photochemical reaction stopped at night. The

Deleted: 7

667 diurnal variation in  $\text{NH}_4^+$  was similar to that in  $\text{NO}_3^-$  due to the acid/base neutralization reaction.  
668 The overlapping of the  $\sigma_{\text{abs,BrC},370\text{nm}}$ ,  $\text{NH}_4^+$  and  $\text{NO}_3^-$  diurnal variations would lead to a significant  
669 correlation between BrC absorption and  $\text{NO}_3^-$  or  $\text{NH}_4^+$ . High concentrations of  $\text{Ca}^{2+}$  and  $\text{Mg}^{2+}$   
670 are often found in dust-related aerosols (Lee et al., 1999).  $\sigma_{\text{abs,BrC},370\text{nm}}$  showed poor correlations  
671 with both  $\text{Ca}^{2+}$  and  $\text{Mg}^{2+}$ , indicating that dust-related aerosol components contribute  
672 insignificantly to the total aerosol mass loading and, thus, dust may not affect the AAE  
673 differentiation method used in this work. Although sulfur dioxide ( $\text{SO}_2$ ) may also be emitted by  
674 biomass burning,  $\text{SO}_4^{2-}$  is often believed to be secondary in nature, and the presence of other  
675 intense  $\text{SO}_2$  sources (e.g., automobile and industrial emissions) further reduces the correlation  
676 between BrC and  $\text{SO}_4^{2-}$ . Sources of  $\text{Cl}^-$  include both combustion and sea salt spray (Waldman  
677 et al., 1991). Although the prevailing wintertime wind direction was from the north, sea salt  
678 can still be carried to the site by a weak sea breeze, and thus,  $\text{Cl}^-$  may not show considerable  
679 correlation with BrC.

### 680 3.4 BrC radiative forcing efficiency

681 The radiative effects of aerosol scattering, BrC absorption, and BC absorption were investigated  
682 by the SBDART model. For each investigated variable under cloud-free conditions, we run the  
683 model twice to calculate the DRF at the TOA with and without the investigated variable.  
684 Accordingly, the difference of  $\Delta F$  between the two simulations was considered as the radiative  
685 effect of the investigated variable. The results showed that the average radiative forcings at the  
686 TOA by scattering, BrC absorption, and BC absorption were  $-21.4 \pm 5.5 \text{ W m}^{-2}$ ,  $2.3 \pm 1.8 \text{ W m}^{-2}$ ,  
687 and  $10.9 \pm 5.1 \text{ W m}^{-2}$ , respectively. Furthermore, BrC absorption was attributed to  $15.8 \pm 4.4\%$   
688 of the warming effect caused by aerosol light absorption, demonstrating the nonnegligible role  
689 of BrC in radiative forcing evaluation.

690 We also calculated the BrC radiative forcing efficiency (RFE) under various  $SSA$  (ranging from  
691 0.7 to 0.99) at three wavelengths, i.e., 440 nm, 675 nm, and 870 nm. The RFE was denoted as  
692 the radiative forcing normalized by the AOD. The average AOD and ASY at the three  
693 wavelengths were 0.365 and 0.691 at 440 nm, 0.212 and 0.632 at 675 nm, and 0.154 and 0.619  
694 at 870 nm, respectively. A solar zenith angle of  $55^\circ$  and an average shortwave broadband surface  
695 albedo (0.119) were used in the calculation. The results were plotted as a set of RFE lookup  
696 charts as a function of the surface BrC absorption contribution (see Fig. 9).

Deleted: 10

698 In general, for any wavelength, the RFE increased with increasing BrC absorption contribution  
699 for a certain *SSA*, indicating that BrC was a more efficient radiative forcing agent due to the  
700 preferential absorbance of BrC in a shorter wavelength range. However, for a certain BrC  
701 absorption contribution, the RFE increased with decreasing *SSA*, i.e., a higher portion of light-  
702 absorbing aerosol components can lead to more efficient radiative forcing. The trend among  
703 panels (a), (b), and (c) in Fig. 9 demonstrated that the effect of BrC absorption contribution on  
704 RFE was wavelength-dependent, i.e., BrC was a weaker radiative forcing agent at longer  
705 wavelengths, which is also consistent with the wavelength-dependent light-absorbing property  
706 of BrC. The red stars in Fig. 9 denote the average *SSA* and BrC absorption contribution  
707 conditions during this campaign, i.e.,  $0.029 \text{ W m}^{-2}$  per unit AOD at 440 nm (Fig. 9a),  $0.007 \text{ W}$   
708  $\text{m}^{-2}$  per unit AOD at 675 nm (Fig. 9b), and  $0.0002 \text{ W m}^{-2}$  per unit AOD at 870 nm (Fig. 9c).  
709 These results suggested that the average value of RFE decreased distinctly from 440 nm to 870  
710 nm not only because of the lower BrC absorption contribution but also because of the  
711 wavelength-dependence of the BrC RFE. It should also be noted that the simulations were based  
712 on *SSA* measured under dry conditions. Under the typical ambient conditions of the PRD, the  
713 *SSA* might be markedly enhanced by aerosol water uptake (Jung et al., 2009), and then, the BrC  
714 radiative forcing efficiency might be less. Moreover, Fig. 9 also serves as a lookup table to  
715 conveniently assess the BrC radiative forcing efficiency at different wavelengths with different  
716 BrC absorption contributions for a certain *SSA*.

#### 717 4 Conclusion

718 In this work, light absorption due to BrC in the PRD region of China was quantitatively deduced  
719 during the winter season of 2014. [The AAE of ambient particles and BC core were derived](#)  
720 [from the measurements. For ambient particles,  \$AAE\_{370-520\text{nm}}\$  and  \$AAE\_{520-880\text{nm}}\$  ranged from 0.81](#)  
721 [to 2.31 and 0.91 to 2.13, respectively. In the case of BC,  \$AAE\_{\text{BC},370-520\text{nm}}\$  and  \$AAE\_{\text{BC},520-880\text{nm}}\$](#)   
722 [ranged from 0.59 to 0.98 and 0.82 to 1.15, respectively.](#) Using the absorption coefficients of  
723 BC calculated according to the Mie theory and the observed total aerosol absorption coefficients,  
724 we estimated the  $AAE_{\text{BC}}$  and hence the BrC absorption contribution for the optically equivalent  
725 mixture configuration. The average BrC light absorption contribution ranged from  $8.7 \pm 4.3\%$  at  
726 660 nm up to  $34.1 \pm 8.0\%$  at 370 nm when  $AAE_{\text{BC}}$  was set as uniform. The sensitivity of  $AAE_{\text{BC}}$   
727 estimation associated with different RI and mixing state assumptions was further investigated.

Deleted: 10

Deleted: 10

Deleted: 10a

Deleted: 10b

Deleted: 10c

Deleted: 10

734 The results showed that variations in the real RI of the non-absorbing material (1.35 to 1.6) may  
735 decrease  $AAE_{BC,370-520nm}$  from 0.84 to 0.87 and  $AAE_{BC,520-880nm}$  from 1.07 to 1.15 for core-shell  
736 mixtures, with an  $AAE_{BC,370-520nm}$  of 0.33 and  $AAE_{BC,520-880nm}$  of 0.63 for external mixtures.  
737 Variations in the core's real RI (1.5 to 2.0) and imaginary RI (0.4 to 1.0) may reduce  $AAE_{BC,370-}$   
738  $520nm$  from 0.55 to 0.99 and  $AAE_{BC,520-880nm}$  from 0.84 to 1.27 for the core-shell mixture and  
739 reduce  $AAE_{BC,370-520nm}$  from 0.04 to 0.45 and  $AAE_{BC,520-880nm}$  from 0.28 to 0.79 for the external  
740 mixture. These results indicate that the optical properties of the BC core and non-absorbing  
741 material can significantly affect the accuracy of  $AAE_{BC}$  and corresponding BrC absorption  
742 contribution estimations. [Compared to the values of BrC light absorption coefficient and BrC](#)  
743 [light absorption contribution from other similar studies conducted in the East Asia region, the](#)  
744 [BrC measured in this work showed relatively lower values of light absorption coefficient but](#)  
745 [was found responsible for relatively higher portion of light absorption.](#)

746 Additionally, the measurements of major water-soluble inorganic ions (including  $K^+$ ,  $NO_3^-$ , and  
747  $NH_4^+$ ) and particulate OC showed consistent features with those of  $\sigma_{abs,BrC,370nm}$ , implying that  
748 BrC was associated with biomass-burning emissions from nearby rural areas. Moreover, the  
749 diurnal trend in  $\sigma_{abs,BrC,370nm}/OC$  indicated that primary biomass burning emissions can produce  
750 intense light-absorbing BrC, while the photochemical aging process may weaken the light-  
751 absorbing capability of BrC.

752 Using a radiative transfer model (i.e., SBDART), we estimated the BrC effects on aerosol  
753 radiative forcing. The average shortwave aerosol direct radiative forcings due to scattering, BrC  
754 absorption, and BC absorption at the TOA were evaluated to be  $-21.4 \pm 5.5 \text{ W m}^{-2}$ ,  $2.3 \pm 1.8 \text{ W}$   
755  $\text{m}^{-2}$ , and  $10.9 \pm 5.1 \text{ W m}^{-2}$ , respectively. BrC absorption accounted for  $15.8 \pm 4.4\%$  of the total  
756 shortwave solar absorption warming effect at the TOA, indicating that BrC might be an  
757 important climate forcing agent, which is largely neglected in current climate models. To  
758 facilitate the estimation of the climate effects of BrC, a set of look-up charts was constructed  
759 for the investigated area based on the default tropical atmosphere profile, average surface  
760 albedo, average asymmetry factor, and surface-measured aerosol properties (i.e., BrC  
761 absorption contribution,  $SSA$ , and AOD). Therefore, the role of the BrC radiative forcing  
762 efficiency at three wavelengths can be conveniently assessed for certain  $SSA$  and BrC  
763 absorption contributions.

764

765 *Author contributions*

766 HT, JZ, YM, and CC designed the experiments, and ZL, LL, YQ, NW, FL, YL, and MC carried  
767 out the field measurements and data analysis. ZL and YQ performed Mie theory simulation.  
768 ZL, JZ, and HT prepared the manuscript with comments from all coauthors.

769

770 *Acknowledgements*

771 This work is supported by the National Key Project of MOST (2016YFC0201901 and  
772 2016YFC0203305), and National Natural Science Foundation of China (41575122 and  
773 41730106). We are also deeply thankful for Dr. Wu and the staff at the Hong Kong Polytechnic  
774 University site of AERONET.

775

776 **References:**

- 777 Andreae, M. O., and Merlet, P.: Emission of trace gases and aerosols from biomass burning,  
778 *Glob. Biogeochem. Cycle*, 15, 955-966, 2001.
- 779 Andreae, M. O., and Gelencser, A.: Black carbon or brown carbon? The nature of light-  
780 absorbing carbonaceous aerosols, *Atmospheric Chemistry & Physics*, 6, 3131-3148, 2006.
- 781 Ångström, A.: On the Atmospheric Transmission of Sun Radiation and on Dust in the Air,  
782 *Geografiska Annaler*, 11, 156-166, 1929.
- 783 Arnott, W. P., Hamasha, K., Moosmüller, H., Sheridan, P. J., and Ogren, J. A.: Towards Aerosol  
784 Light-Absorption Measurements with a 7-Wavelength Aethalometer: Evaluation with a  
785 Photoacoustic Instrument and 3-Wavelength Nephelometer, *Aerosol Science and Technology*,  
786 39, 17-29, 10.1080/027868290901972, 2005.
- 787 Arola, A., Schuster, G. L., Pitkänen, M. R. A., Dubovik, O., Kokkola, H., Lindfors, A. V.,  
788 Mielonen, T., Raatikainen, T., Romakkaniemi, S., Tripathi, S. N., and Lihavainen, H.: Direct  
789 radiative effect by brown carbon over the Indo-Gangetic Plain, *Atmospheric Chemistry and  
790 Physics*, 15, 12731-12740, 10.5194/acp-15-12731-2015, 2015.
- 791 Bauer, J. J., Yu, X.-Y., Cary, R., Laulainen, N., and Berkowitz, C.: Characterization of the  
792 Sunset Semi-Continuous Carbon Aerosol Analyzer, *Journal of the Air & Waste Management  
793 Association*, 59, 826-833, 10.3155/1047-3289.59.7.826, 2012.
- 794 Bodhaine, B. A.: Aerosol absorption measurements at Barrow, Mauna Loa and the south pole,  
795 *Journal of Geophysical Research Atmospheres*, 100, 8967-8975, 1995.

- 796 Bohren, C. F., and Huffman, D. R.: Wiley: Absorption and Scattering of Light by Small  
797 Particles - Craig F. Bohren, Donald R. Huffman, Optics & Laser Technology, 31, 328-328, 1983.
- 798 Bohren, C. F., and Huffman, D. R.: Absorption and Scattering of Light by Small Particles,  
799 WILEY - VCH Verlag GmbH & Co. KGaA 328-328 pp., 2007.
- 800 Bond, T. C., Streets, D. G., Yarber, K. F., Nelson, S. M., Woo, J. H., and Klimont, Z.: A  
801 technology-based global inventory of black and organic carbon emissions from combustion, J.  
802 Geophys. Res.-Atmos., 109, 43, 10.1029/2003jd003697, 2004.
- 803 Bond, T. C., Zarzycki, C., Flanner, M. G., and Koch, D. M.: Quantifying immediate radiative  
804 forcing by black carbon and organic matter with the Specific Forcing Pulse, Atmospheric  
805 Chemistry and Physics, 11, 1505-1525, 10.5194/acp-11-1505-2011, 2011.
- 806 Bricaud, A., and Morel, A.: Light attenuation and scattering by phytoplanktonic cells: a  
807 theoretical modeling, Applied Optics, 25, 571, 10.1364/ao.25.000571, 1986.
- 808 Burling, I. R., Yokelson, R. J., Akagi, S. K., Urbanski, S. P., Wold, C. E., Griffith, D. W. T.,  
809 Johnson, T. J., Reardon, J., and Weise, D. R.: Airborne and ground-based measurements of the  
810 trace gases and particles emitted by prescribed fires in the United States (vol 11, pg 12197,  
811 2011), Atmospheric Chemistry and Physics, 12, 103-103, 10.5194/acp-12-103-2012, 2012.
- 812 Chan, C. K., and Yao, X.: Air pollution in mega cities in China, Atmospheric Environment, 42,  
813 1-42, <http://dx.doi.org/10.1016/j.atmosenv.2007.09.003>, 2008.
- 814 Cheng, Y., He, K. B., Zheng, M., Duan, F. K., Du, Z. Y., Ma, Y. L., Tan, J. H., Yang, F. M., Liu,  
815 J. M., Zhang, X. L., Weber, R. J., Bergin, M. H., and Russell, A. G.: Mass absorption efficiency  
816 of elemental carbon and water-soluble organic carbon in Beijing, China, Atmospheric  
817 Chemistry and Physics, 11, 11497-11510, 10.5194/acp-11-11497-2011, 2011.
- 818 Cheng, Y. F., Eichler, H., Wiedensohler, A., Heintzenberg, J., Zhang, Y. H., Hu, M., Herrmann,  
819 H., Zeng, L. M., Liu, S., Gnauk, T., Brüggemann, E., and He, L. Y.: Mixing state of elemental  
820 carbon and non-light-absorbing aerosol components derived from in situ particle optical  
821 properties at Xinken in Pearl River Delta of China, Journal of Geophysical Research:  
822 Atmospheres, 111, doi:10.1029/2005JD006929, 2006.
- 823 Cheung, H. H. Y., Tan, H., Xu, H., Li, F., Wu, C., Yu, J. Z., and Chan, C. K.: Measurements of  
824 non-volatile aerosols with a VTDMA and their correlations with carbonaceous aerosols in  
825 Guangzhou, China, Atmospheric Chemistry and Physics, 16, 8431-8446, 10.5194/acp-16-  
826 8431-2016, 2016.
- 827 Coen, M. C., Weingartner, E., Apituley, A., Ceburnis, D., Fierzschmidhauser, R., Flentje, H.,  
828 Henzing, J. S., Jennings, S. G., Moerman, M., and Petzold, A.: Minimizing light absorption  
829 measurement artifacts of the Aethalometer: evaluation of five correction algorithms,  
830 Atmospheric Measurement Techniques, 3, 457-474, 2010.
- 831 Desyaterik, Y., Sun, Y., Shen, X., Lee, T., Wang, X., Wang, T., and Collett, J. L.: Speciation of

832 "brown" carbon in cloud water impacted by agricultural biomass burning in eastern China,  
833 *Journal of Geophysical Research: Atmospheres*, 118, 7389-7399, 10.1002/jgrd.50561, 2013.

834 Drinovec, L., Močnik, G., Zotter, P., Prévôt, A. S. H., Ruckstuhl, C., Coz, E., Rupakheti, M.,  
835 Sciare, J., Müller, T., Wiedensohler, A., and Hansen, A. D. A.: The "dual-spot" Aethalometer:  
836 an improved measurement of aerosol black carbon with real-time loading compensation,  
837 *Atmospheric Measurement Techniques*, 8, 1965-1979, 10.5194/amt-8-1965-2015, 2015.

838 Erlick, C., Abbatt, J. P. D., and Rudich, Y.: How Different Calculations of the Refractive Index  
839 Affect Estimates of the Radiative Forcing Efficiency of Ammonium Sulfate Aerosols, *Journal*  
840 *of the Atmospheric Sciences*, 68, 1845-1852, 10.1175/2011jas3721.1, 2011.

841 Feng, X., Dang, Z., Huang, W., Shao, L., and Li, W.: Microscopic morphology and size  
842 distribution of particles in PM<sub>2.5</sub> of Guangzhou City, *J Atmos Chem*, 64, 37-51,  
843 10.1007/s10874-010-9169-7, 2010.

844 Feng, Y., Ramanathan, V., and Kotamarthi, V. R.: Brown carbon: a significant atmospheric  
845 absorber of solar radiation?, *Atmospheric Chemistry and Physics*, 13, 8607-8621, 10.5194/acp-  
846 13-8607-2013, 2013.

847 Hoffer, A., Gelencsér, A., Guyon, P., and Kiss, G.: Optical properties of humic-like substances  
848 (HULIS) in biomass-burning aerosols, *Atmospheric Chemistry & Physics*, 5, 3563-3570, 2005.

849 Holben, B. N., Eck, T. F., Slutsker, I., Tanré, D., Buis, J. P., Setzer, A., Vermote, E., Reagan, J.  
850 A., Kaufman, Y. J., and Nakajima, T.: AERONET—A Federated Instrument Network and Data  
851 Archive for Aerosol Characterization, *Remote Sensing of Environment*, 66, 1-16, 1998.

852 Huang, R.-J., Zhang, Y., Bozzetti, C., Ho, K.-F., Cao, J.-J., Han, Y., Daellenbach, K. R., Slowik,  
853 J. G., Platt, S. M., Canonaco, F., Zotter, P., Wolf, R., Pieber, S. M., Bruns, E. A., Crippa, M.,  
854 Ciarelli, G., Piazzalunga, A., Schwikowski, M., Abbaszade, G., Schnelle-Kreis, J.,  
855 Zimmermann, R., An, Z., Szidat, S., Baltensperger, U., Haddad, I. E., and Prévôt, A. S. H.:  
856 High secondary aerosol contribution to particulate pollution during haze events in China,  
857 *Nature*, 514, 218-222, 10.1038/nature13774, 2014.

858 Jiang, D., Wang, C., Wu, D., Deng, X., Huang, X., Tan, H., Li, F., and Deng, T.: Diurnal  
859 variation of atmospheric boundary layer over Wushan station, Guangzhou using wind profiler  
860 radar (in Chinese), *Journal of Tropical Meteorology*, 29, 129-135, 2013.

861 Jung, J., Lee, H., Kim, Y. J., Liu, X., Zhang, Y., Gu, J., and Fan, S.: Aerosol chemistry and the  
862 effect of aerosol water content on visibility impairment and radiative forcing in Guangzhou  
863 during the 2006 Pearl River Delta campaign, *Journal of Environmental Management*, 90, 3231-  
864 3244, <http://dx.doi.org/10.1016/j.jenvman.2009.04.021>, 2009.

865 Katrinak, K. A., Rez, P., Perkes, P. R., and Buseck, P. R.: Fractal geometry of carbonaceous  
866 aggregates from an urban aerosol, *Environmental Science & Technology*, 27, págs. 225-238,  
867 1993.

868 Khalizov, A. F., Xue, H., Wang, L., Zheng, J., and Zhang, R.: Enhanced light absorption and  
869 scattering by carbon soot aerosol internally mixed with sulfuric acid, *The journal of physical*  
870 *chemistry. A*, 113, 1066-1074, 10.1021/jp807531n, 2009.

871 Kirchstetter, T. W., Novakov, T., and Hobbs, P. V.: Evidence that the spectral dependence of  
872 light absorption by aerosols is affected by organic carbon, *Journal of Geophysical Research:*  
873 *Atmospheres*, 109, n/a-n/a, 10.1029/2004jd004999, 2004.

874 Kulkarni, P., Baron, P. A., and Willeke, K.: *Aerosol measurement : principles, techniques, and*  
875 *applications*, Van Nostrand Reinhold, 807-808 pp., 1996.

876 Lack, D. A., and Cappa, C. D.: Impact of brown and clear carbon on light absorption  
877 enhancement, single scatter albedo and absorption wavelength dependence of black carbon,  
878 *Atmospheric Chemistry and Physics*, 10, 4207-4220, 10.5194/acp-10-4207-2010, 2010.

879 Lack, D. A., and Langridge, J. M.: On the attribution of black and brown carbon light absorption  
880 using the Ångström exponent, *Atmospheric Chemistry and Physics*, 13, 10535-10543,  
881 10.5194/acp-13-10535-2013, 2013.

882 Lai, S.-c., Zou, S.-c., Cao, J.-j., Lee, S.-c., and Ho, K.-f.: Characterizing ionic species in PM2.5  
883 and PM10 in four Pearl River Delta cities, South China, *Journal of Environmental Sciences*, 19,  
884 939-947, [https://doi.org/10.1016/S1001-0742\(07\)60155-7](https://doi.org/10.1016/S1001-0742(07)60155-7), 2007.

885 Laskin, A., Laskin, J., and Nizkorodov, S. A.: Chemistry of atmospheric brown carbon, *Chem*  
886 *Rev*, 115, 4335-4382, 10.1021/cr5006167, 2015.

887 Lee, E., Chan, C. K., and Paatero, P.: Application of positive matrix factorization in source  
888 apportionment of particulate pollutants in Hong Kong, *Atmospheric Environment*, 33, 3201-  
889 3212, [https://doi.org/10.1016/S1352-2310\(99\)00113-2](https://doi.org/10.1016/S1352-2310(99)00113-2), 1999.

890 Levine, J.: Biomass Burning Aerosols in a Savanna Region of the Ivory Coast, *French Forum*,  
891 235-236, 1991.

892 Li, H., Han, Z., Cheng, T., Du, H., Kong, L., Chen, J., Zhang, R., and Wang, W.: Agricultural  
893 Fire Impacts on the Air Quality of Shanghai during Summer Harvesttime, *Aerosol and Air*  
894 *Quality Research*, 10.4209/aaqr.2009.08.0049, 2010.

895 Lin, P., Hu, M., Deng, Z., Slanina, J., Han, S., Kondo, Y., Takegawa, N., Miyazaki, Y., Zhao,  
896 Y., and Sugimoto, N.: Seasonal and diurnal variations of organic carbon in PM2.5 in Beijing  
897 and the estimation of secondary organic carbon, *Journal of Geophysical Research*, 114,  
898 10.1029/2008jd010902, 2009.

899 Liu, C., Chung, C. E., Yin, Y., and Schnaiter, M.: The absorption Ångström exponent of black  
900 carbon: from numerical aspects, *Atmospheric Chemistry and Physics*, 18, 6259-6273,  
901 10.5194/acp-18-6259-2018, 2018.

902 Liu, D., Taylor, J. W., Young, D. E., Flynn, M. J., Coe, H., and Allan, J. D.: The effect of

903 complex black carbon microphysics on the determination of the optical properties of brown  
904 carbon, *Geophysical Research Letters*, 42, 613-619, 2015.

905 Liu, L., Mishchenko, M. I., and Patrick Arnott, W.: A study of radiative properties of fractal  
906 soot aggregates using the superposition T-matrix method, *Journal of Quantitative Spectroscopy  
907 and Radiative Transfer*, 109, 2656-2663, 10.1016/j.jqsrt.2008.05.001, 2008.

908 Ma, N., Zhao, C. S., Müller, T., Cheng, Y. F., Liu, P. F., Deng, Z. Z., Xu, W. Y., Ran, L., Nekat,  
909 B., van Pinxteren, D., Gnauk, T., Müller, K., Herrmann, H., Yan, P., Zhou, X. J., and  
910 Wiedensohler, A.: A new method to determine the mixing state of light absorbing carbonaceous  
911 using the measured aerosol optical properties and number size distributions, *Atmos. Chem.  
912 Phys.*, 12, 2381-2397, 10.5194/acp-12-2381-2012, 2012.

913 Ma, Y., Li, S. Z., Zheng, J., Khalizov, A., Wang, X., Wang, Z., and Zhou, Y. Y.: Size-resolved  
914 measurements of mixing state and cloud-nucleating ability of aerosols in Nanjing, China, *J.  
915 Geophys. Res.-Atmos.*, 122, 9430-9450, 10.1002/2017jd026583, 2017.

916 Mie, G.: *Beitrage Zur Optik Truber Medien, Speziell Kolloidaler Metallosungen*, *Annalen Der  
917 Physik*, 25, 377, 1908.

918 Moosmüller, H., Chakrabarty, R. K., Ehlers, K. M., and Arnott, W. P.: Absorption Ångström  
919 coefficient, brown carbon, and aerosols: basic concepts, bulk matter, and spherical particles,  
920 *Atmospheric Chemistry and Physics*, 11, 1217-1225, 10.5194/acp-11-1217-2011, 2011.

921 Nakayama, T., Ikeda, Y., Sawada, Y., Setoguchi, Y., Ogawa, S., Kawana, K., Mochida, M.,  
922 Ikemori, F., Matsumoto, K., and Matsumi, Y.: Properties of light - absorbing aerosols in the  
923 Nagoya urban area, Japan, in August 2011 and January 2012: Contributions of brown carbon  
924 and lensing effect, *Journal of Geophysical Research Atmospheres*, 119, 12,721-712,739, 2015.

925 Olson, M. R., Victoria Garcia, M., Robinson, M. A., Van Rooy, P., Dietenberger, M. A., Bergin,  
926 M., and Schauer, J. J.: Investigation of black and brown carbon multiple-wavelength-dependent  
927 light absorption from biomass and fossil fuel combustion source emissions, *Journal of  
928 Geophysical Research: Atmospheres*, 120, 6682-6697, 10.1002/2014jd022970, 2015.

929 Pio, C. A., Legrand, M., Alves, C. A., Oliveira, T., Afonso, J., Caseiro, A., Puxbaum, H.,  
930 Sanchez-Ochoa, A., and Gelencsér, A.: Chemical composition of atmospheric aerosols during  
931 the 2003 summer intense forest fire period, *Atmospheric Environment*, 42, 7530-7543, 2008.

932 Qin, Y. M., Tan, H. B., Li, Y. J., Li, Z. J., Schurman, M. I., Liu, L., Wu, C., and Chan, C. K.:  
933 Chemical characteristics of brown carbon in atmospheric particles at a suburban site near  
934 Guangzhou, China, *Atmospheric Chemistry and Physics Discussions*, 1-23, 10.5194/acp-2018-  
935 730, 2018.

936 Redmond, H., and Thompson, J. E.: Evaluation of a quantitative structure-property relationship  
937 (QSPR) for predicting mid-visible refractive index of secondary organic aerosol (SOA),  
938 *Physical chemistry chemical physics : PCCP*, 13, 6872-6882, 10.1039/c0cp02270e, 2011.

939 Ricchiazzi, P., Yang, S., Gautier, C., and Sowle, D.: SBDART: A Research and Teaching  
940 Software Tool for Plane-Parallel Radiative Transfer in the Earth's Atmosphere, *Bulletin of the*  
941 *American Meteorological Society*, 79, 2101-2114, 10.1175/1520-  
942 0477(1998)079<2101:Sarats>2.0.Co;2, 1998.

943 Roesch, A.: Use of Moderate-Resolution Imaging Spectroradiometer bidirectional reflectance  
944 distribution function products to enhance simulated surface albedos, *Journal of Geophysical*  
945 *Research*, 109, 10.1029/2004jd004552, 2004.

946 Sareen, N., Schwier, A. N., Shapiro, E. L., Mitroo, D., and McNeill, V. F.: Secondary organic  
947 material formed by methylglyoxal in aqueous aerosol mimics, *Atmospheric Chemistry and*  
948 *Physics*, 10, 997-1016, 10.5194/acp-10-997-2010, 2010.

949 Satish, R., Shamjad, P., Thamban, N., Tripathi, S., and Rastogi, N.: Temporal Characteristics of  
950 Brown Carbon over the Central Indo-Gangetic Plain, *Environ Sci Technol*, 51, 6765-6772,  
951 10.1021/acs.est.7b00734, 2017.

952 Scarnato, B. V., Nielsen, K., Vahidinia, S., and Richard, D.: Effect of Aggregation and Mixing  
953 on optical properties of Black Carbon, 2013.

954 Schmid, O., Artaxo, P., Arnott, W. P., Chand, D., Gatti, L. V., Frank, G. P., Hoffer, A., Schnaiter,  
955 M., and Andreae, M. O.: Spectral light absorption by ambient aerosols influenced by biomass  
956 burning in the Amazon Basin. I: Comparison and field calibration of absorption measurement  
957 techniques, *Atmos. Chem. Phys.*, 6, 3443-3462, 10.5194/acp-6-3443-2006, 2006.

958 Segura, S., Estellés, V., Titos, G., Lyamani, H., Utrillas, M. P., Zotter, P., Prévôt, A. S. H.,  
959 Močnik, G., Alados-Arboledas, L., and Martínez-Lozano, J. A.: Determination and analysis of  
960 in situ spectral aerosol optical properties by a multi-instrumental approach, *Atmospheric*  
961 *Measurement Techniques*, 7, 2373-2387, 10.5194/amt-7-2373-2014, 2014.

962 Seinfeld, J. H., and Pandis, S. N.: *Atmospheric Chemistry and Physics*, John Wiley & Sons, Inc,  
963 New York, 1998.

964 Stokes, G. M., and Schwartz, S. E.: The Atmospheric Radiation Measurement (ARM) Program:  
965 Programmatic Background and Design of the Cloud and Radiation Test Bed, *Bulletin of the*  
966 *American Meteorological Society*, 75, 1201-1221, 1994.

967 T. C. Bond, †, M. Bussemer, B. Wehner, S. Keller, R. J. Charlson, a., and Heintzenberg‡, J.:  
968 Light Absorption by Primary Particle Emissions from a Lignite Burning Plant, *Environmental*  
969 *Science & Technology*, 33, 3887-3891, 1999.

970 Tan, H., Liu, L., Fan, S., Li, F., Yin, Y., Cai, M., and Chan, P. W.: Aerosol optical properties and  
971 mixing state of black carbon in the Pearl River Delta, China, *Atmospheric Environment*, 131,  
972 196-208, <http://dx.doi.org/10.1016/j.atmosenv.2016.02.003>, 2016a.

973 Tan, H., Yin, Y., Li, F., Liu, X., Chan, P. W., Deng, T., Deng, X., Wan, Q., and Wu, D.:  
974 Measurements of particle number size distributions and new particle formations events during

975 winter in the Pearl River Delta region, China, *Journal of Tropical Meteorology*, 22, 191-199,  
976 10.16555/j.1006-8775.2016.02.009, 2016b.

977 Waldman, J. M., Lioy, P. J., Zelenka, M., Jing, L., Lin, Y. N., He, Q. C., Qian, Z. M., Chapman,  
978 R., and Wilson, W. E.: Wintertime measurements of aerosol acidity and trace elements in  
979 Wuhan, a city in central China, *Atmospheric Environment. Part B. Urban Atmosphere*, 25, 113-  
980 120, [https://doi.org/10.1016/0957-1272\(91\)90045-G](https://doi.org/10.1016/0957-1272(91)90045-G), 1991.

981 Wang, J., Nie, W., Cheng, Y., Shen, Y., Chi, X., Wang, J., Huang, X., Xie, Y., Sun, P., Xu, Z.,  
982 Qi, X., Su, H., and Ding, A.: Light absorption of brown carbon in eastern China based on 3-  
983 year multi-wavelength aerosol optical property observations and an improved absorption  
984 Ångström exponent segregation method, *Atmospheric Chemistry and Physics*, 18, 9061-9074,  
985 10.5194/acp-18-9061-2018, 2018.

986 Washenfelder, R. A., Attwood, A. R., Brock, C. A., Guo, H., Xu, L., Weber, R. J., Ng, N. L.,  
987 Allen, H. M., Ayres, B. R., and Baumann, K.: Biomass burning dominates brown carbon  
988 absorption in the rural southeastern United States, *Geophysical Research Letters*, 42, 653-664,  
989 2015.

990 Wex, H., Neusüß, C., Wendisch, M., Stratmann, F., Koziar, C., Keil, A., Wiedensohler, A., and  
991 Ebert, M.: Particle scattering, backscattering, and absorption coefficients: An in situ closure  
992 and sensitivity study, *Journal of Geophysical Research Atmospheres*, 107, LAC-1-LAC 4-18,  
993 2002.

994 Wu, C., Wu, D., and Yu, J. Z.: Quantifying black carbon light absorption enhancement with  
995 a novel statistical approach, *Atmospheric Chemistry and Physics*, 18, 289-309, 10.5194/acp-  
996 18-289-2018, 2018.

997 Wu, D., Mao, J., Deng, X., Tie, X., Zhang, Y., Zeng, L., Li, F., Tan, H., Bi, X., Huang, X., Chen,  
998 J., and Deng, T.: Black carbon aerosols and their radiative properties in the Pearl River Delta  
999 region, *Science in China Series D: Earth Sciences*, 52, 1152-1163, 10.1007/s11430-009-0115-  
1000 y, 2009.

1001 Xie, C., Xu, W., Wang, J., Wang, Q., Liu, D., Tang, G., Chen, P., Du, W., Zhao, J., Zhang, Y.,  
1002 Zhou, W., Han, T., Bian, Q., Li, J., Fu, P., Wang, Z., Ge, X., Allan, J., Coe, H., and Sun, Y.:  
1003 Vertical characterization of aerosol optical properties and brown carbon in winter in urban  
1004 Beijing, China, *Atmospheric Chemistry and Physics Discussions*, 1-28, 10.5194/acp-2018-788,  
1005 2018.

1006 Yu, J., Yan, C., Liu, Y., Li, X., Zhou, T., and Zheng, M.: Potassium: A Tracer for Biomass  
1007 Burning in Beijing?, *Aerosol and Air Quality Research*, 18, 2447-2459,  
1008 10.4209/aaqr.2017.11.0536, 2018.

1009 Yuan, J. F., Huang, X. F., Cao, L. M., Cui, J., Zhu, Q., Huang, C. N., Lan, Z. J., and He, L. Y.:  
1010 Light absorption of brown carbon aerosol in the PRD region of China, *Atmospheric Chemistry  
1011 and Physics*, 16, 1433-1443, 10.5194/acp-16-1433-2016, 2016a.

1012 Yuan, L., Yin, Y., Xiao, H., Yu, X., Hao, J., Chen, K., and Liu, C.: A closure study of aerosol  
1013 optical properties at a regional background mountainous site in Eastern China, *Science of The*  
1014 *Total Environment*, 550, 950-960, 10.1016/j.scitotenv.2016.01.205, 2016b.

1015 Zhang, Y., Li, Z., Sun, Y., Lv, Y., and Xie, Y.: Estimation of atmospheric columnar organic  
1016 matter (OM) mass concentration from remote sensing measurements of aerosol spectral  
1017 refractive indices, *Atmospheric Environment*, 179, 107-117, 10.1016/j.atmosenv.2018.02.010,  
1018 2018.

1019 Zhou, S., Wang, T., Wang, Z., Li, W., Xu, Z., Wang, X., Yuan, C., Poon, C. N., Louie, P. K. K.,  
1020 Luk, C. W. Y., and Wang, W.: Photochemical evolution of organic aerosols observed in urban  
1021 plumes from Hong Kong and the Pearl River Delta of China, *Atmospheric Environment*, 88,  
1022 219-229, 10.1016/j.atmosenv.2014.01.032, 2014.

1023  
1024

1025 **Table 1.** Inter-comparison of the performance of various Mie-calculation schemes. The base  
 1026 case is based on the empirical distribution function and mixing states of BC particles obtained  
 1027 from previous field measurements at the same site.  $\Phi_{N,CV}$  denotes the portion of non-BC  
 1028 particles and  $r_{ext}$  is the mass portion of externally mixed BC with respect to total BC.  $AAE_{BC}$  is  
 1029 the absorption Ångström exponent of BC, and the subscript represents the wavelength range.  
 1030  $Abs_{BrC,370\%}$  and  $Abs_{BrC,520\%}$  are the BrC absorption contributions at 370 nm and 520 nm,  
 1031 respectively.  $Calcabs_{880}$  is the calculated absorption at 880 nm using Mie model.  $Measabs_{880}$  is  
 1032 the measured absorption by an Aethalometer at 880 nm.  $b$  is the intercept of the regression  
 1033 analysis between  $Measabs_{880}$  and  $Calcabs_{880}$ , i.e.,  $Calcabs_{880}=b * Measabs_{880}$ .  $R^2$  is the  
 1034 correlation coefficient of the equation. The refractive index of BC core ( $\tilde{m}_{core}$ ) and nonlight-  
 1035 absorbing particles ( $\tilde{m}_{non}$ ) is set to be  $1.80-0.54i$  and  $1.55-10^{-7}i$ , respectively (Tan et al., 2016a),

Case #	Scheme	$\Phi_{N,CV}$	$r_{ext}$	AAE BC,370-520	AAE BC,520-880	Abs BrC,370 %	Abs BrC,520 %	Calc abs <sub>880</sub>	Meas abs <sub>880</sub>	b	R <sup>2</sup>
Base		0.384 to 0.137	0.58	0.723	0.962	34.13%	15.96%	21.869		1.019	0.979
1		0	1	0.331	0.626	51.64%	29.57%	15.832		0.747	0.968
2		0	0	0.856	1.128	24.76%	8.28%	27.827		1.295	0.976
3		0	0.58	0.745	0.974	33.22%	15.46%	21.936	<b>21.199</b>	1.029	0.979
4		0.384 to 0.137	0	0.835	1.111	26.01%	9.14%	27.302		1.269	0.975
5		0.5	0	0.778	1.043	29.96%	12.30%	24.921		1.150	0.968
6		0.5	0.58	0.674	0.928	36.39%	17.49%	20.897		0.977	0.975

1036

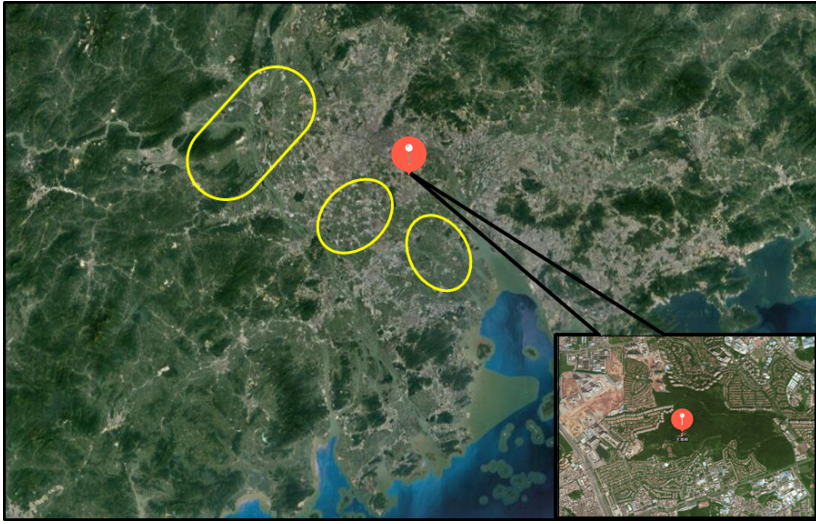
1037

1038

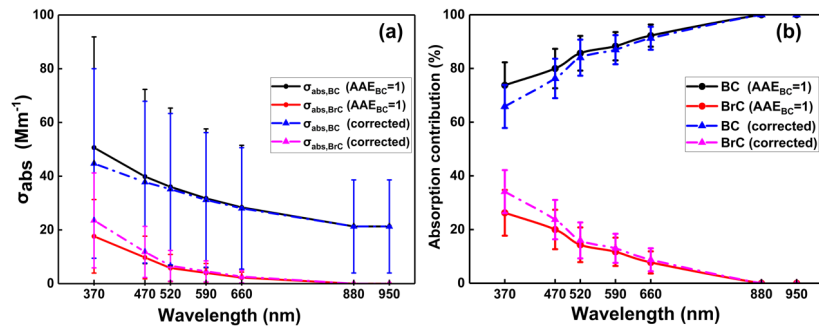
1039 **Table 2.** Observational studies of the BrC light absorption coefficient and contribution in the  
 1040 near-ultraviolet wavelength range in East Asia.

Periods	Location	$\lambda$ (nm)	Mean BrC absorption coefficient	Mean BrC absorption contribution	Instrument	Reference
Nov. 2014 – Jan. 2015	Guangzhou (China)	370	17.6 Mm <sup>-1</sup> 23.5 Mm <sup>-1</sup>	26.2% (AAE <sub>BC</sub> =1) 34.1% (corrected)	Aethalometer r AE-33	This study
Jan. 2014 – Feb. 2014; Sep. 2014 – Oct. 2014	Shenzhen (China)	405	3.0 Mm <sup>-1</sup> 1.4 Mm <sup>-1</sup>	11.7% (winter) 6.3% (fall)	PASS-3	Yuan et al. (2016a)
Nov. 2014	Heshan (China)	405	3.9 Mm <sup>-1</sup>	12.1%	PASS-3	Yuan et al. (2016a)
Nov. 2016 – Dec. 2016	Beijing (China)	370	106.4 Mm <sup>-1</sup> 93.8 Mm <sup>-1</sup>	46% (at the ground) 48% (at 260 m)	Aethalometer r AE-33	Xie et al. (2018)
Jun. 2013 – May. 2016	Nanjing (China)	370	35.8 Mm <sup>-1</sup>	16.7%	Aethalometer r AE-31	Wang et al. (2018)
Jan. 2012	Nagoya (Japan)	405	Not detected	11% (300°C) 17% (400°C)	Thermometer r PASS-3	(Nakayama et al. (2015))

1041



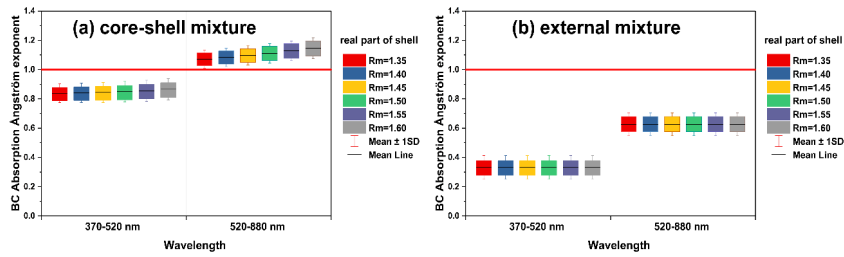
1042  
1043 Figure 1. The location of Panyu station (CAWNET) in the PRD region (indicated by the red  
1044 dot). The plain areas within the yellow circles are the main rural areas of western PRD.  
1045



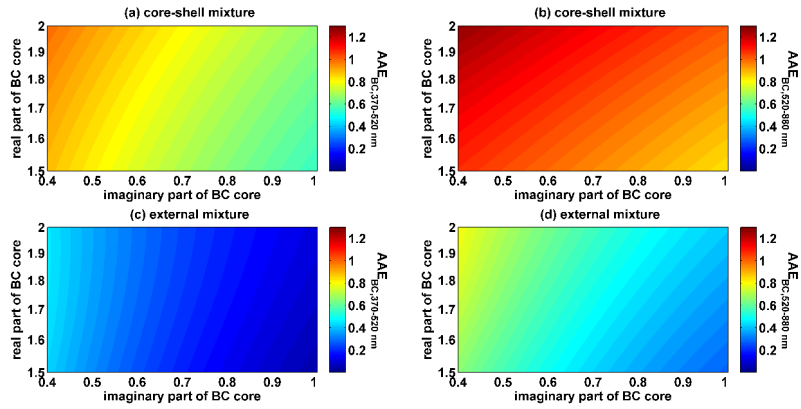
1047

1048 Figure 2. (a) BC and BrC particle average light absorption coefficients at different  
 1049 wavelengths under different AAE<sub>BC</sub> assumptions; the whiskers represent an error of  
 1050 one standard deviation. (b) Contributions of BC and BrC to the total light absorption  
 1051 coefficient at different wavelengths under different AAE<sub>BC</sub> assumptions; the whiskers  
 1052 represent an error of one standard deviation.

1053

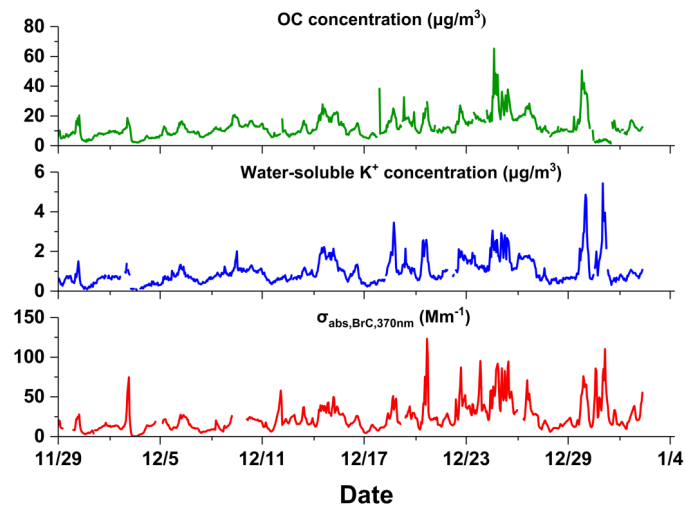


1054 Figure 3. Influence of the wavelength-independent refractive index of the non-  
 1055 absorbing materials on the (a) AAEs of the core-shell mixture and (b) AAEs of the  
 1056 external mixture with a constant BC core refractive index ( $\tilde{m}_{core}=1.80-0.54i$ ). The  
 1057 imaginary part of the non(less)-absorbing shell was set to  $10^{-7}$ , while the real part varied  
 1058 from 1.35 to 1.60. In each panel, the boundaries of the box represent the 75th and 25th  
 1059 percentiles; the whiskers above and below each box indicate an error of one standard  
 1060 deviation; the black lines in the boxes denote the average values. In panels a and b, the  
 1061 red line indicates where  $AAE_{BC}=1$ .  
 1062

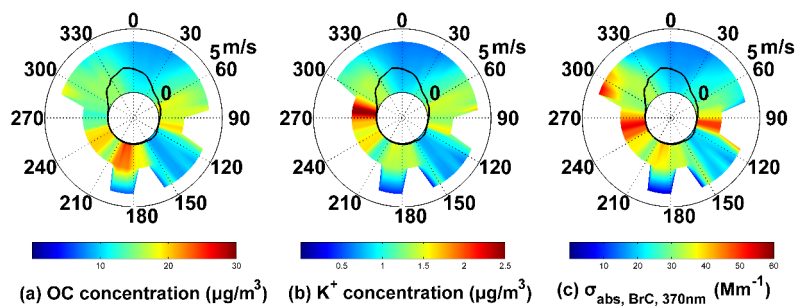


1064

1065 Figure 4. Influence of the wavelength-independent refractive index of the BC core on  
 1066 AAEs with a constant shell refractive index ( $\tilde{m}_{shell} = 1.55 - 10^{-7}i$ ). A core-shell mixture  
 1067 was used for panels a and b, and an external mixture was used for panels c and d. The  
 1068 real part of  $\tilde{m}_{core}$  varied from 1.5 to 2.0, with a step of 0.05, and the imaginary part of  
 1069  $\tilde{m}_{core}$  varied from 0.4 to 1.0, with a step of 0.05.  
 1070



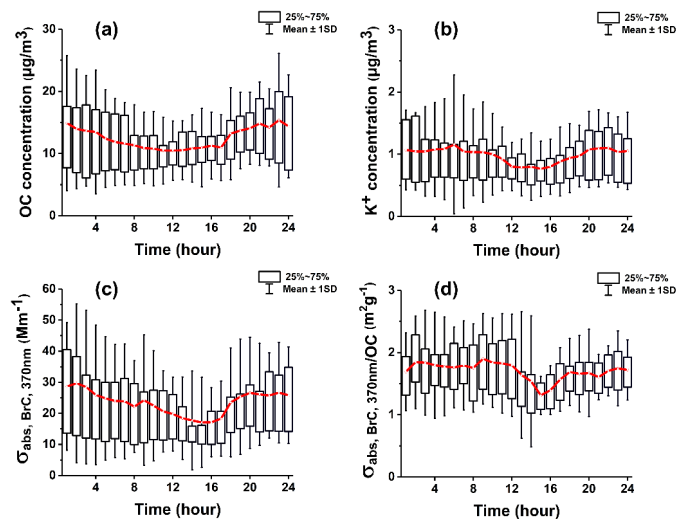
1071  
1072 Figure 5. Time series of the OC aerosol mass concentration (green line), water-soluble  $\text{K}^+$  mass  
1073 concentration (blue line), and BrC light absorption (red line).  
1074



1076

1077 Figure 6. Wind rose plots of OC (a),  $\text{K}^+$  (b), and  $\sigma_{\text{abs, BrC, 370nm}}$  (c). In each panel, the black solid  
 1078 lines denote the frequency of the wind direction. The shaded contour represents the average  
 1079 values of the corresponding species for that wind speed (radial length) and wind direction  
 1080 (transverse direction) in polar coordinates.

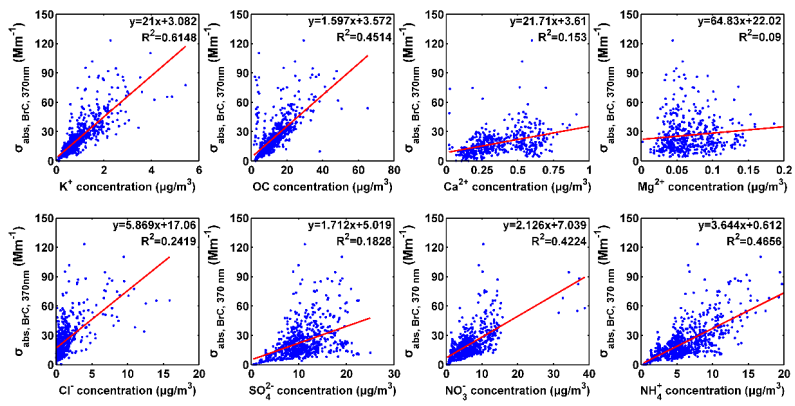
1081



1083

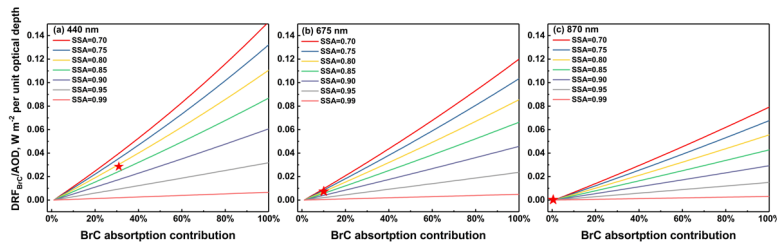
1084 Figure 7. Box-whisker plots of diurnal trends in the OC concentration (a), water-soluble  $\text{K}^+$   
 1085 concentration (b),  $\sigma_{\text{abs, BrC, 370nm}}$  (c), and  $\sigma_{\text{abs, BrC, 370nm}}/\text{OC}$  (d). The red traces represent the  
 1086 variation in the average value. The upper and lower boundaries of the box represent the 75th  
 1087 and 25th percentiles, respectively; the whiskers above and below each box represent an error  
 1088 of one standard deviation.

1089



1090

1091 Figure 8. Correlations of the BrC absorption coefficient at 370 nm with OC, water-soluble  $\text{K}^+$ ,  
 1092  $\text{Ca}^{2+}$ ,  $\text{Mg}^{2+}$ , Cl $^-$ ,  $\text{SO}_4^{2-}$ ,  $\text{NO}_3^-$ , and  $\text{NH}_4^+$  aerosol concentrations.



1093

1094 Figure 9. BrC radiative forcing efficiencies, which are defined as the BrC TOA direct radiative  
 1095 forcing divided by the AOD, as a function of the BrC to BC absorption ratio and *SSA* measured  
 1096 at the surface. The average AOD of the three wavelengths, the average ASY of the three  
 1097 wavelengths, a solar zenith angle of 55°, and average shortwave broadband surface albedo were  
 1098 used in the calculation. The red star corresponds to the average *SSA* and BrC absorption  
 1099 contributions determined from this campaign.

Deleted: 10

<b>Page 17: [1] Deleted</b>	<b>JZ</b>	<b>7/20/19 1:11:00 PM</b>
We want to		
<b>Page 17: [1] Deleted</b>	<b>JZ</b>	<b>7/20/19 1:11:00 PM</b>
We want to		
<b>Page 17: [1] Deleted</b>	<b>JZ</b>	<b>7/20/19 1:11:00 PM</b>
We want to		
<b>Page 17: [1] Deleted</b>	<b>JZ</b>	<b>7/20/19 1:11:00 PM</b>
We want to		
<b>Page 17: [1] Deleted</b>	<b>JZ</b>	<b>7/20/19 1:11:00 PM</b>
We want to		
<b>Page 17: [1] Deleted</b>	<b>JZ</b>	<b>7/20/19 1:11:00 PM</b>
We want to		
<b>Page 17: [1] Deleted</b>	<b>JZ</b>	<b>7/20/19 1:11:00 PM</b>
We want to		
<b>Page 17: [1] Deleted</b>	<b>JZ</b>	<b>7/20/19 1:11:00 PM</b>
We want to		
<b>Page 17: [1] Deleted</b>	<b>JZ</b>	<b>7/20/19 1:11:00 PM</b>
We want to		
<b>Page 17: [1] Deleted</b>	<b>JZ</b>	<b>7/20/19 1:11:00 PM</b>
We want to		
<b>Page 17: [1] Deleted</b>	<b>JZ</b>	<b>7/20/19 1:11:00 PM</b>
We want to		
<b>Page 17: [2] Deleted</b>	<b>JZ</b>	<b>7/20/19 1:05:00 PM</b>
acquire		
<b>Page 17: [2] Deleted</b>	<b>JZ</b>	<b>7/20/19 1:05:00 PM</b>
acquire		
<b>Page 17: [2] Deleted</b>	<b>JZ</b>	<b>7/20/19 1:05:00 PM</b>

acquire

Page 17: [2] Deleted	JZ	7/20/19 1:05:00 PM
----------------------	----	--------------------

acquire

Page 17: [2] Deleted	JZ	7/20/19 1:05:00 PM
----------------------	----	--------------------

acquire

Page 17: [2] Deleted	JZ	7/20/19 1:05:00 PM
----------------------	----	--------------------

acquire

Page 17: [2] Deleted	JZ	7/20/19 1:05:00 PM
----------------------	----	--------------------

acquire

Page 17: [3] Deleted	JZ	7/20/19 1:19:00 PM
----------------------	----	--------------------

running the repeated

Page 17: [3] Deleted	JZ	7/20/19 1:19:00 PM
----------------------	----	--------------------

running the repeated

Page 17: [3] Deleted	JZ	7/20/19 1:19:00 PM
----------------------	----	--------------------

running the repeated

Page 17: [3] Deleted	JZ	7/20/19 1:19:00 PM
----------------------	----	--------------------

running the repeated

Page 17: [3] Deleted	JZ	7/20/19 1:19:00 PM
----------------------	----	--------------------

running the repeated

Page 17: [3] Deleted	JZ	7/20/19 1:19:00 PM
----------------------	----	--------------------

running the repeated

Page 17: [3] Deleted	JZ	7/20/19 1:19:00 PM
----------------------	----	--------------------

running the repeated

Page 17: [3] Deleted	JZ	7/20/19 1:19:00 PM
----------------------	----	--------------------

running the repeated

Page 17: [3] Deleted	JZ	7/20/19 1:19:00 PM
----------------------	----	--------------------

running the repeated

Page 17: [3] Deleted	JZ	7/20/19 1:19:00 PM
----------------------	----	--------------------

running the repeated

Page 17: [3] Deleted	JZ	7/20/19 1:19:00 PM
----------------------	----	--------------------

running the repeated

<b>Page 17: [4] Deleted</b>	<b>JZ</b>	<b>7/20/19 1:44:00 PM</b>
possible values for the input parameters		
<b>Page 17: [4] Deleted</b>	<b>JZ</b>	<b>7/20/19 1:44:00 PM</b>
possible values for the input parameters		
<b>Page 17: [5] Formatted</b>	<b>JZ</b>	<b>7/20/19 1:49:00 PM</b>
Font:11 pt, Font color: Text 1, Complex Script Font: 11 pt		
<b>Page 17: [5] Formatted</b>	<b>JZ</b>	<b>7/20/19 1:49:00 PM</b>
Font:11 pt, Font color: Text 1, Complex Script Font: 11 pt		
<b>Page 17: [5] Formatted</b>	<b>JZ</b>	<b>7/20/19 1:49:00 PM</b>
Font:11 pt, Font color: Text 1, Complex Script Font: 11 pt		
<b>Page 17: [5] Formatted</b>	<b>JZ</b>	<b>7/20/19 1:49:00 PM</b>
Font:11 pt, Font color: Text 1, Complex Script Font: 11 pt		
<b>Page 17: [5] Formatted</b>	<b>JZ</b>	<b>7/20/19 1:49:00 PM</b>
Font:11 pt, Font color: Text 1, Complex Script Font: 11 pt		